REPORT DOCUMENTATION PAGE

The public reporting burden for this collection of information is estimated to average 1 hour per response, including the time for reviewing instructions, searching existing data sources, gathering and maintaining the data needed, and completing and reviewing the collection of information. Send comments regarding this burden estimate or any other aspect of this collection of information, including suggestions for reducing the burden, to Department of Defense, Washington Headquarters Services, Directorate for Information Operations and Reports (0704-0188), 1215 Jefferson Davis Highway, Suite 1204, Arlington, VA 22202-4302. Respondents should be aware that notwithstanding any other provision of law, no person shall be subject to any penalty for failing to comply with a collection of information if it does not display a currently valid OMB control number.
PLEASE DO NOT RETURN YOUR FORM TO THE ABOVE ADDRESS.

1. REPORT DATE (DD-MM-YYYY)	2. REPORT TYPE	3. DATES COVERED (From - To)
29-05-2012	Final Technical Report	1 Mar 2008 - 28 Feb 2012

4. TITLE AND SUBTITLE	5a. CONTRACT NUMBER
Real Time Detecting and Processing Signals by an Integrated Sensor Chip Based on Meta-materials and photonic crystals	
	5b. GRANT NUMBER N00014-08-1-0348
	5c. PROGRAM ELEMENT NUMBER

6. AUTHOR(S)	5d. PROJECT NUMBER
Prather, Dennis W.	
	5e. TASK NUMBER
	5f. WORK UNIT NUMBER

7. PERFORMING ORGANIZATION NAME(S) AND ADDRESS(ES)	8. PERFORMING ORGANIZATION REPORT NUMBER
University of Delaware 210 Hullihen Hall Newark, DE 19716	ELEG332262-053112

9. SPONSORING/MONITORING AGENCY NAME(S) AND ADDRESS(ES)	10. SPONSOR/MONITOR'S ACRONYM(S)
Office of Naval Research 875 North Randolph Street Arlington, VA 22203-1995	
	11. SPONSOR/MONITOR'S REPORT NUMBER(S)

12. DISTRIBUTION/AVAILABILITY STATEMENT

Approved for Public Release; distribution is Unlimited

20120601059

13. SUPPLEMENTARY NOTES

14. ABSTRACT

This effort has been realized to advance the U.S. Navy's vision of an integrated ship topside, where the elements detecting, guiding, processing, and radiating signals become an integral part of the ship's structure. The integrated signal processing structure must also meet structural and design requirements: signature control, isolation, weight reduction, and a low observable (LO) profile. To fulfill these requirements, several different technological phases are used including dielectric waveguides and transitions, radiating grating structures, and advanced artificial materials, namely, photonic crystals (PhCs) and meta-materials. The dielectric waveguides, and PhC devices are electromagnetically transparent, leading to a significant reduction of the scattering cross-section, i.e., better signature control. Also, the PhC structure provides very good signal isolation and is lightweight while maintaining structural soundness. Spatial light modulators with tunable metamaterials allow for signal processing while maintaining a LO profile. To support integrated signal detecting and processing system, designs, simulations, and experimental results for the years 2008-2012 are presented.

15. SUBJECT TERMS

meta-materials; photonic crystals; negative refraction; phase modulators

16. SECURITY CLASSIFICATION OF:			17. LIMITATION OF ABSTRACT	18. NUMBER OF PAGES	19a. NAME OF RESPONSIBLE PERSON
a. REPORT	b. ABSTRACT	c. THIS PAGE	UU	37	Dennis Prather
U	U	U			**19b. TELEPHONE NUMBER (Include area code)** 302-831-8170

Real Time Detecting and Processing Signals by an Integrated Sensor Chip Based on Meta-materials and Photonic Crystals

by

Professor Dennis W. Prather
Technical Point of Contact

University of Delaware
Department of Electrical and Computer Engineering
Newark, DE 19716
Phone: (302) 831-8170
Fax: (302) 831-8172
Email: dprather@ee.udel.edu

Date: May 29, 2012

Table of Contents

1   Abstract:

This effort has been realized to advance the U.S. Navy's vision of an integrated ship topside, where the elements detecting, guiding, processing, and radiating signals become an integral part of the ship's structure. This integrated signal processing structure must also meet structural and design requirements such as: signature control, isolation, weight reduction, and a low observable (LO) profile. To fulfill these requirements we utilize several different technological phases including dielectric waveguides and transitions, radiating grating structures, and advanced artificial materials, namely, photonic crystals (PhC's) and meta-materials. The dielectric waveguides, and PhC devices are electromagnetically transparent, which leads to a significant reduction of the scattering cross-section, i.e., better signature control. Additionally, the PhC structure provides very good signal isolation and is light weight while maintaining structural soundness. The spatial light modulators with tunable metamaterials allow for signal processing while maintaining a LO profile. To help achieve the vision of this integrated signal detecting and processing system, we present our designs, simulations, and experimental results for the years 2008-2012.

2   Introduction

A critical capability in the modern warfare environment is to rapidly and accurately detect and process electronic warfare signals. However, the spectrum of such signals is increasing rapidly, which stresses the limits of current and next generation technology. In addition, there is also a pressing problem with limited space and location for such processors as well as accommodating the numerous radiating apertures that are needed to intercept the signals. For this reason, there are significant efforts underway that aim to construct highly sensitive and compact systems by integrating multiple functions into the superstructure such that the sensor can directly capture and process signals. This process is difficult to solve using conventional electronic-based sensing systems due to the space and power requirements of the requisite devices and systems.

To address these requirements, new and novel technologies need to be developed. One possible means to accomplish this is to use advanced artificial materials, namely, photonic crystals and meta-materials, to construct the integrated signal detecting and processing system. This system will be based on the unique dispersion properties of photonic crystals, which will be used to achieve waveguiding and correlation. The main advantage of this approach over conventional techniques is that these devices are, to a large extent, electromagnetically transparent and therefore have a significantly reduced signature. The photonic crystal components also permit the realization of RF structures on a scale comparable to the RF wavelength, which enables the design of waveguides and antennas that are light in weight and compact in size. The self-collimating design that we have employed for this PhC waveguide also offers very good signal isolation due to its low out-of-plane scattering and is energy efficient due to its low propagation loss. In addition, we have designed a hybrid dielectric waveguide/transition coupler to transfer electromagnetic energy in and out of the PhC. This Input/Output (I/O) couplers provide an efficient means to transfer electromagnetic energy to and from the PhC while producing a small signature.

3

This effort also includes the design of a spatial light modulator (SLM) based on tunable meta-materials. A SLM is attractive in the RF/microwave frequency domain as it can have applications in phased array antennas and radars for beam-forming and beam scanning. For our integrated design, this SLM allows us to process the detected signals while maintaining a low observable (LO) profile. Additionally, in our future work for this project we plan to implement a dielectric grating structure that will allow us to radiate a modulated signal from our integrated chip. **Figure 1**, provides a visual notion of our complete system.
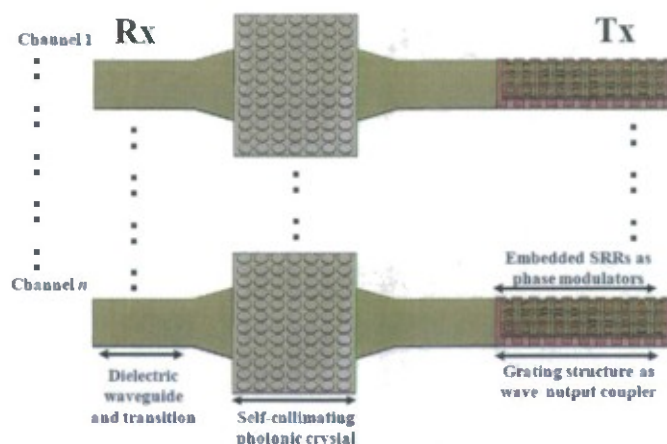

Figure 1. *Integrated Signal Processing Modules with Artificially Engineered Materials*

To this end, in this effort we designed, fabricated, and demonstrated a compact integrated sensor chip based on photonic crystals and metamaterials that can be used directly for detecting, channeling, and processing signals, which we detail in the following sections.

3 Summary of Project Achievements/ Deliverables

a) Designed, fabricated and tested a self-collimating PhC waveguide

b) Designed, modeled and experimentally demonstrated an efficient self-collimating PhC coupling technique

c) Demonstrated numerically and experimentally a spatial light modulator using tunable meta-materials

d) Published two refereed journal papers and one conference paper reporting the results of the spatial light modulators using tunable meta-materials

e) Designed a High- Index Contrast (HIC) Self Collimating Photonic Crystal (SCPhC) to demonstrate superior self-collimation using ceramic rods and polyutherane foam

f) Simulated HIC PhC using the 2D Finite Difference Time Domain (FDTD) method where a transmission loss of 0.011 dB/λ, i.e., 0.4 dB/m was noted

g) Performed 2D scans of both the Low-Index Contrast (LIC) and HIC PhCs, confirming self-collimation in the X-band

h) The 2D scan for HIC PhC demonstrated better wave confinement compared to the LIC PhC

i) Comparative transmission analysis for the LIC and HIC showed an improvement by a factor of 2 for the HIC PhC

j) Published one conference paper reporting self-collimation in LIC PhC
k) Designed a "fishnet" metamaterial which exhibits left-handed behavior around 1.5um wavelength using the Finite Difference Time Domain (FDTD) method
l) Developed a CMOS compatible fabrication process for the realization of the simulated structure
m) Developed a dual-beam Michelson interferometer setup to characterize the fabricated samples
n) Published 2 peer-reviewed journal paper and one conference paper describing the fabrication and characterization process of the 'fishnet' metamaterials

## 4   Detailed Milestone Achievements

4.1   Photonic Crystal Waveguide

The underlying physics of this approach, to design a PhC waveguide, is based on the unique dispersion properties of PhC's. PhC's are passive devices that consist of periodic arrays of localized structures, whose material constants, differ from that of the host material. A unique quality of the PhC is its ability to spatially and spectrally control and propagate electromagnetic waves, which provides wide bandwidth, high capability, small size, light weight and low cost for signal processing systems.   Conventionally, photonic bandgaps, i.e., defect-based photonic crystals, have been used to attain strong confinement of light within the photonic crystal. For this project, we exploit an alternative PhC structure that does not require defects for confinement of light and yet can arbitrarily route light. These structures are said to exhibit self-collimating behavior primarily due to their low out-of-plane scattering (which also results in good signal isolation), and they are also capable of very low propagation loss when implemented in slab photonic crystals.

4.1.1   Dispersion Engineering of Photonic Crystals

The dispersion of photonic crystals can be considerably more varied than that of materials found in nature due to the phenomena caused by the coherent interactions of an electromagnetic wave with a periodic structure. In order to engineer the dispersive properties of photonic crystal, the resulting dispersion surfaces must be extracted. A dispersion surface represents a solution to Maxwell's equation in the entire Brillouin zone. The dispersion diagram, as seen in Figure 2(a), is a plot of several bands for k-points that trace the perimeter of the irreducible Brillouin zone. The dispersion diagram coupled with the important relationship between group velocity, v_g, and the gradient of $\omega(k)$, $v_g(k_0) = \nabla_k \omega(k)$, which describes how a wave packet propagates in a

medium, provide the conceptual tools used to study the behavior of light in photonic crystals. The image in Figure 2(*b*) is realized by mounting several dispersion surfaces vertically in the ω direction. The diagram in Figure 2 (*b*) is then a family of surfaces, where each horizontal section represents an equifrequency contour (EFC) and each interception between a dispersion surface and the constant-*k* line represents a single mode at different frequencies that can exist within the lattice.

(a)   (b)
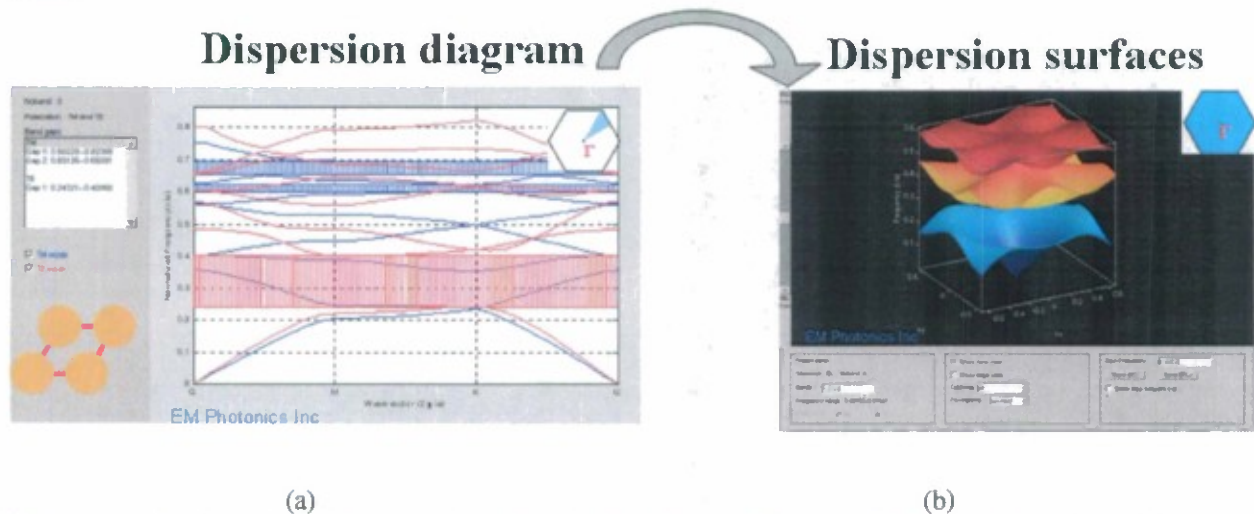
Figure 2. *(a)Two-dimensional dispersion diagram, (b) three-dimensional view of the dispersion surfaces. These diagrams are the main tools use for dispersion engineering of PhC's.*

4.1.2   Design of Self-collimating Photonic Crystal

For most on-chip applications electromagnetic energy is necessarily emitted in narrow beams, which implies the presence of a *k*-vector perpendicular to the propagation direction. As a result, a beam of electromagnetic energy must diverge as it travels through space in a linear, homogeneous, isotropic material. Figure 3(*a*) illustrates the dispersion surfaces in such a material, whose equifrequency contour (EFC) are circular. Metallic waveguides have generally been used to contain the diverging beams in such materials, but since the standard metallic waveguide does not fulfill the requirements for our project, we designed a self-collimating PhC that reduces the diverging behavior. This nonmetallic form of waveguiding is realized by designing a lattice with a narrow range of group velocity directions. If one were to design a material with a square EFC as the one seen in Figure 3(*b*), then the group velocities would have the same direction, perpendicular to a side of the square EFC. Although a perfectly square EFC is elusive, to say the least, a contour like the one in Figure 3(*b*) is achievable with a square-lattice PhC like the one used for our self-collimating design.
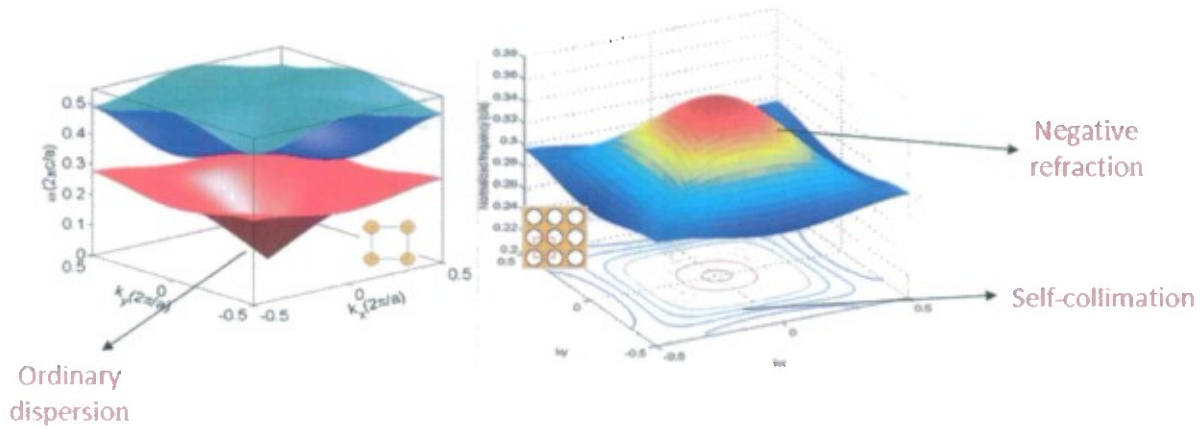
Figure 3. *Dispersion surfaces, (a) for a homogeneous unpatterned slab; (b) for a homogeneous square- lattice self-collimating PhC slab.*

The self-collimating PhC design also reduces the out-of-plane radiation compared to band-gap PhC's. In the case of band-gap PhC's some modes may lie above the light cone due to the degeneracy of defect modes; therefore, some of the energy may be transferred to the modes lying above the light cone. In the case of the self-collimating PhC no modes lie above the light cone at their self-collimating frequency; therefore, very little energy is radiated out-of-plane. Given the above considerations, we can see that a self-collimating PhC performs the waveguiding requirements for this project, while also offering very good signal isolation and energy efficiency due to its low out-of-plane radiation and low propagation loss. In the following sections we will report on the design and experimental results of this device.

4.1.3   Dielectric Input/Output (I/O) Couplers for Waveguide Transition

It was also necessary to design a structure to couple the detected signal to the PhC with the minimum mismatch loss possible. We studied several different options to fulfill this requirement including rectangular metallic waveguides and rectangular dielectric slab waveguides. These waveguides did not yield the desired coupling efficiency since the energy transferred to the PhC still exhibited a diverging behavior, which resulted in a large mismatch at the transition with the PhC. To improve the coupling efficiency, we designed a hybrid dielectric waveguide with a tapered transition, as pictured in **Figure 4**, to couple electromagnetic energy in and out of the PhC. This Input/Output (I/O) couplers provide an efficient means to transfer electromagnetic energy to and from the PhC while producing a small signature.
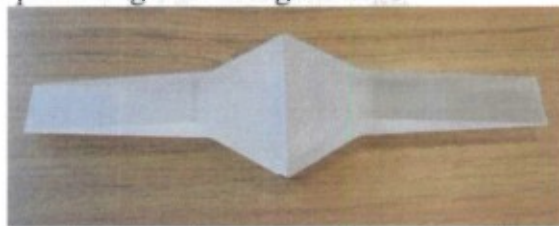
Figure 4. *Dielectric waveguide with tapered transition*

4.1.4   Numerical and Experimental Results for Self-Collimating PhC

It is often necessary to resort to numerical methods to solve electromagnetic problems due to the high level of complication that they involve. Because the modulation of photonic crystals is at the wavelength level, our design is no exception; hence, we resorted to numerical methods such as the Plane Wave Expansion Method (PWEM), the Finite-Difference Time-Domain Method (FDTD), and the Finite Element Method (FEM). We used PWEM and FDTD to solve for the photonic band structure in order to determine the appropriate lattice parameters for our self-collimating photonic crystals (PhC). Once the PhC had been designed, we used a commercial full-wave FEM simulation software to simulate and integrate the elements of our signal processing system.

After all the different elements of our integrated system were fully designed, we fabricated the photonic crystals and coupling structures in order to perform the experimental verification of our numerical results. In our experimental setup we employed a Vector Network Analyzer (VNA), 3.5 mm coaxial cables, and two X-band square waveguides to feed a signal to the PhC through the I/O couplers and to measure the outgoing signal. In this section we present an overview of the numerical simulations and experimental results for our self-collimating photonic crystal waveguide.

We used the FEM software to simulate a butt-coupled connection between the I/O couplers as seen in figure 2.4. We were able to simulate an insertion loss between the I/O couplers to $S_{21} >$ -0.6 dB . Based on this design, we fabricated the I/O couplers (**Figure 4**) with a polystyrene dielectric (ε =1.59) using an automated milling machine. The insertion loss between the couplers was measured experimentally to $S_{21} > $ -1.2 dB in the X frequency band. These results are presented graphically in **Figure 5**.

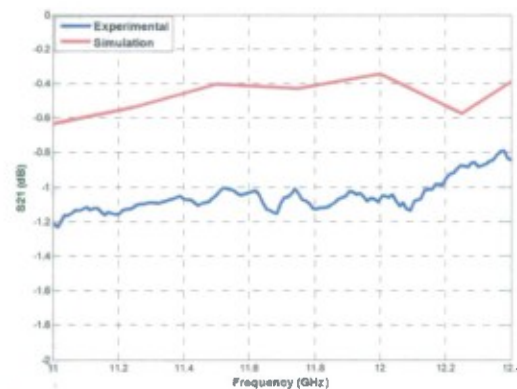**Figure 5.** *Electric field distribution at 12 GHz*

**Figure 6.** *Results for butt-coupled I/O couplers*

We also simulated an integrated system including the I/O couplers and a 24" self-collimating PhC. The best simulation results were achieved with the I/O couplers shifted into the PhC slab and the coupler fused to the first lattice of the PhC, as seen in Figure 6. The results from this simulation yielded an insertion loss = -2.8 dB @ 12 GHz. We used a CNC router to fabricate the PhC lattice on an Eccostock polyurethane foam with Rexolite rods filling the periodically located holes as seen in **Figure 7**. We then experimentally measured the insertion loss through the self-collimating PhC, yielding S_{21} = -3.29 dB through a 12" PhC at 12.1 GHz. Figure 8graphically presents simulation and experimental results for the self-collimating PhC integrated with I/O couplers.

Figure 7 *Simulated self-collimating PhC and its electric field distribution at 12 GHz*


Figure 8 *Fabricated self-collimating PhC with shifted I/O couplers*
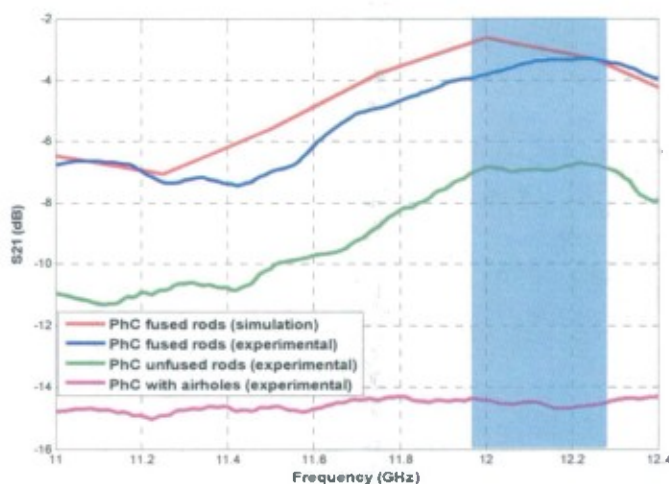

Figure 9. *Numerical and experimental results for self-collimating PhC*

We also needed to determine and isolate the coupling and transmission loss components in our PhC-based system, so we experimentally measured the insertion loss for PhC slabs of different lengths. The results for this measurements are presented in Figure 9. Using the measurements in Figure 9 we interpolated a line of insertion loss for PhC's of different lengths as seen in figure 2.10. We also extrapolated a data point from the line in figure 2.10 that provides a value for the total coupling loss, $2 L_c = -1.9 dB$, independent of PhC length, i.e., for an infinitesimal PhC length. This result allowed us to compute the unilateral coupling loss component, $L_c = -0.95$ dB. Using these extrapolation technique we also determined the transmission loss component of the photonic crystal, $L_t = -0.12$ dB/λ, i.e., -0.12 dB/inch at 12.1 GHz.
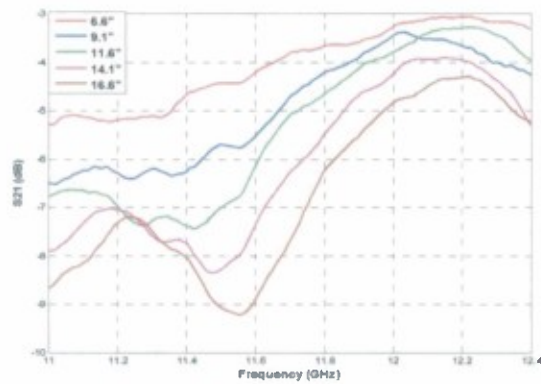
Figure 10 *Insertion loss for PhC slabs of different lengths*
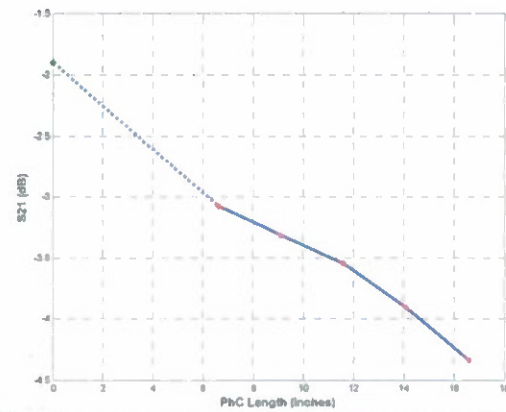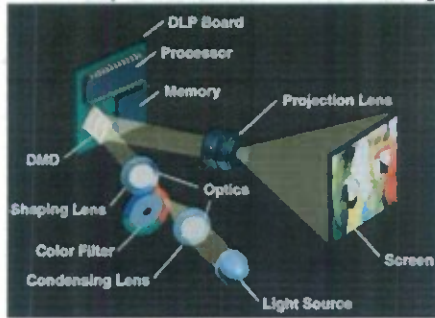

Figure 11 *Interpolated line for insertion loss 12.1 GHz*

4.2 Compact Spatial Light Modulator Using Tunable Metamaterial

In this task, we explored the possibilities of RF/photonics applications based on metamaterials. The ability of metamaterials to respond to an electromagnetic field and bring about changes in a material's fundamental properties has opened up doors for new applications such as the flat lens, antenna miniaturization and artificial magnetic conductors to name a few. One of the advantages of these artificial materials is that they can also be tuned over a frequency range by effectively changing the substrate properties, the geometry of the resonating metamaterial structure, or by changing the external fields with non-linear dielectrics. To further emphasize, a tunable phase modulator is attractive in the RF/microwave frequency domain as it can have applications in phased array antennas and radars for beam-forming and beam scanning. Moreover, it has the potential to set the platform for a spatial light modulator (SLM) in this frequency regime.

Figure 12. *A Digital Light Processing (DLP)-based projector utilizing spatial light modulation technique. Source:(http://www.pctechguide.com /images/57DLP_1chip.jpg)*

SLMs can be primarily of two types, based on the method of modulation: amplitude and phase. Amplitude modulators usually operate in the reflective mode whereas the phase modulators operation is in the transmission mode thus making them more efficient in terms of energy consumption. As mentioned earlier, their applicability in RF/microwave frequency regime could be diverse; hence, a route to developing one with enhanced features is essential. Along that line, we envision that metamaterials can play a critical role in the development process as shown in Figure 13. The modulator will be made out of clusters of metamaterials, namely, the metapixels (MPs) that can be arranged on a planar substrate material. Each MP is a group of dual split rings stacked in layers that can be thought of as a pixel on a charge coupled device (CCD). These MPs can be individually addressed via electrical connections in terms of voltage or current that will lead to a change in the refractive index of the MP. Also, each MP can have a unique property or phase based on the electrical signal it receives. As a result, an incoming beam can now be modulated as it passes through our array of MPs, or the phase modulator.

The key to a successful light modulating device is the tunable element, or in our case a tunable Dual Split Ring Resonators (DSRR). One of the advantages of the Split Ring Resonator (SRR) is that it can be engineered to provide desired enhanced electromagnetic properties. The frequency dispersive nature of the SRRs can be exploited to obtain resonances at desired frequencies. Furthermore, the resonance can be 'turned off' by shorting the gaps of the rings. Modulation can also be brought about using electrical connections such as varactors to switch between the two states of the DSRRs. We plan to implement a common electrical connection to a set of DSRRs to simplify the switching operation. In the following section, we will highlight the reconfigurability properties of the SRRs.

11
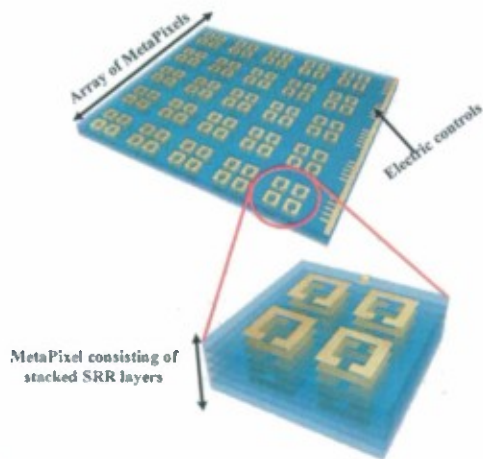
Figure 13 *An envisioned metamaterial-based phase modulator*
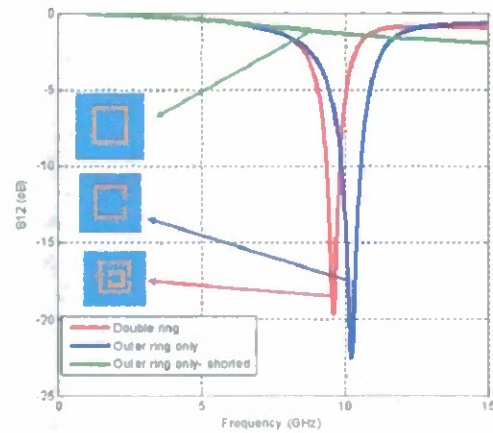
Figure 14 *A simple example of a tunable SRR*

A simple example is considered in Figure 13, where different tunable options are examined of a typical SRR by studying the transmission properties for different cases of the split rings. A unit cell of SRR was excited by a magnetic field perpendicular to the ring. At first, the resonating behavior of a typical SRR is noted by the red curve in Figure 13. Following that, with the omission of the inner ring, there was an upward shift in the resonant frequency. This is due to the fact that, the resonant frequency is inversely proportional to the capacitance. As such, with the omission of the inner ring, the capacitance between the two rings was eliminated, which resulted in an increase in the resonant frequency. Finally, in the third case, the resonance was eliminated altogether as shown in Figure 13 with the green curve. The 'short' of the gap in the outer ring essentially eliminated the capacitance thus effectively removing the resonance of the ring. This simple example highlights the fact that the SRRs can be easily designed to be an efficient tunable structure that can be controlled by manipulating the capacitance of the rings.

As these tunable structures are also scalable with the wavelength, they can be designed for modulation for a desired frequency range. In particular, a Terahertz modulator, where the metamaterials can be grown on a conductive substrate such as GaAs, the amplitude of the incoming wave can be modulated using electrical controls to change the resistivity of the substrate. Also, a major challenge in working with metamaterials has been the inherent loss that arises from their resonating nature. To address such issues, in this task we propose for a phase only modulation using tunable metamaterials, namely the DSRRs. We plan to mitigate the issue of material loss by employing thin resonating metamaterials operating at an off-resonant frequency of the DSRRs to demonstrate a high degree of phase modulation with very minimal loss.

The key advantages of our designs will be the constituent elements, which could be readily manufactured using standard lithography processes, and simple electrical connections could be used to regulate between the two states of the modulation using very thin layers of DSRRs in the propagation direction. Compared to conventional phase modulators, metamaterial-based phase modulators operating in transmission mode, promise to produce enhanced phase modulation in terms of exhibiting a high degree of phase change within a small volume. Moreover, being

physically small it can ensure ease of structural integration and can offer scalability with wavelength that can reduce design constraints while operating in different frequencies. We believe these modulators can be the building block for spatial light modulators in the microwave frequency regime that can add significant advantage over conventional modulators by simplifying future Digital Micromirror Devices (DMD) and phased array antenna design by controlling each element of the array or pixel electronically.

4.2.1   Numerical Results on Metamaterial-based Phase Modulation
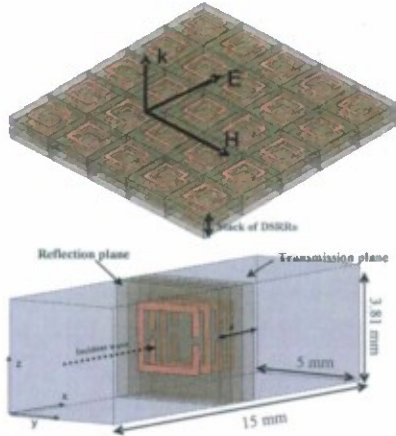
Figure 15 *Configuration for the planar DSRR slab. K-vector is perpendicular to the slab.*

In this section, we briefly overview the numerical setup of DSRRs for calculating the phase modulation. The setup is shown in Figure 15, where the two layers of DSRRs were printed on a FR4 substrate (ε =4.4). The structure was excited by the electric field which was parallel to the gap of the rings with the k-vector perpendicular to the structure. The total thickness of the stack was only 3 mm. The simulated structure was put in a computational region with dimensions of 15 mm x 5 mm x 3.81 mm. The reflection and transmission parameters extracted from the simulation were employed to locate and calculate the effective index of the slab at an off-resonance frequency. In particular, the resonance of the stacked DSRRs occurred at a frequency of 9.15 GHz which provided an effective index of 4.9 for the open state and 3.3 for the closed state at an off-resonant frequency of 8.69 GHz. The index contrast between the two states of the rings produced a phase variation according to $\Delta\phi = (\Delta n_{eff})kd$. For this configuration, the resulting parameters were the following:

$$\Delta n_{eff} = 4.9 - 3.3 = 1.6, \qquad d = \frac{3}{34.5}\lambda, \qquad \Delta\phi \sim 1.6 \times 2\pi / \lambda \times 0.1\lambda \approx \pi/3.$$

We verified this data by using the volumetric electric field information inside the computational region. This method was effective in the sense that it would account for any of multiple reflections that might occur within the slab and would provide the phase information in the free-space after exiting the slab. Phase information was extracted in the propagating x-direction at the 15 mm mark where the wave was in the free-space region after passing through the slab. The calculated phase difference was 140 – 80 degrees = 60 degrees, upon switching between the open and closed rings, as shown in **Figure 16**. In the following section we will discuss the experimental setup and the measured data results.
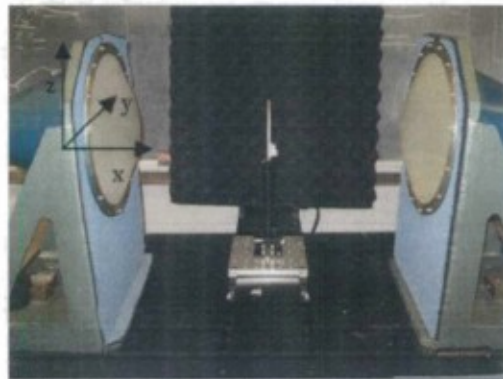
13
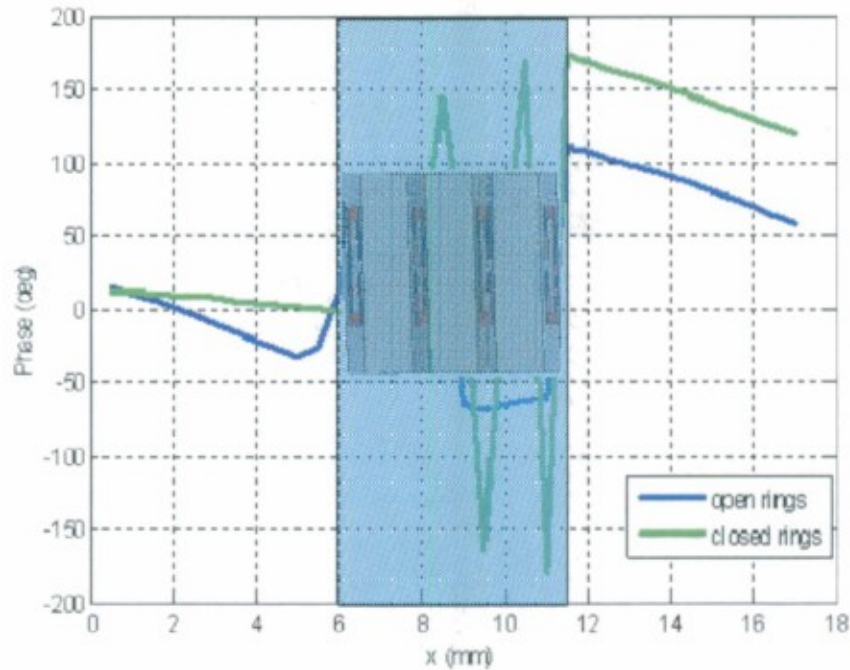
Figure 16. *Plot of the electric field line across the computational region. Shaded region indicates the region occupied by the structure.*

4.2.2 Experimental Results for Phase Modulation using DSRRs

In our free-space experimental measurement setup we utilized two spot-focusing horn lens antennas as the transmitting and receiving antennas, coaxial cables and a Vector Network Analyzer (VNA) for measuring the transmission/reflection parameters. The spot focusing antennas (model no. 857012X-950/C) manufactured by Alpha Industries, Woburn, Ma (USA), operates in the X-band frequency range. Two equal plano-convex lenses were mounted back to back in a conical horn antenna as shown in Figure 17, with one of them responsible for producing an electromagnetic plane wave while the other was responsible for focusing it. The f/# = f/D, where the ratio of focal length (f) of the lens to antenna diameter (D), is equal to 1 and D is approximately 30.5 cm.

Figure 17. *Scanning setup consisting of the DSRR slab mounted on an y-axis translational stage and two spot focusing lens horn antennas.*

The ring designs were exposed on the pre-sensitized FR4 substrate using the standard lithography process; they were then developed and finally the copper was etched by implementing a wet process. A zoomed-in version of the DSSR slab is shown in **Figure 16**. The slabs were 300 mm in length

14

and 150 mm in width, half being occupied by closed rings and the other half occupied by the open rings. The calibration ensured that initially there was zero phase variation and accounted for the transmission loss between the spot focusing lenses.

The sample was first characterized in terms of transmission for the open rings to locate the resonance of the DSRRs in its open state. This was done by bringing the center of the open rings to the center of the lens and measuring the S_{21} parameters with the VNA connected to the setup through a WR90 coax-to-waveguide connector. Based on the transmission data, we chose to operate at an off-resonant frequency of 8.488 GHz where the transmission loss for both configurations was relatively low.

With the chosen operating frequency, we then opted to measure the phase variation that would occur upon transitioning from closed to open rings. We performed a 1-D scan of the slab that would effectively record the phase and amplitude variation. The setup for the 1-D scan was similar to the characterization setup with the only distinction of having the sample mounted on a translational stage along the y-axis as shown in Figure 18. The mounted slab was moved across and in between the two spot focusing antennas by means of our 1-D scanning system. At 8.488 GHz, the distance between the slab and the antenna was one focal length. Within the slab, each section of the closed and open rings was 150 mm x 150 mm which was illuminated completely by the spot focusing lens as the 3dB bandwidth for both E and H field were ($\sim 3\lambda_0 \sim 107$ mm). The E-field was polarized in the z-direction while the slab was scanned in the y axis for 300 mm with a step size of 1.5 mm. Precautions were taken for the unwarranted shaking of the sample as it was translated across by giving few seconds in between each scan so that the sample would stabilize and avoid possible errors. The measured scanned data is shown in Figure 18 where the phase changes were noted to be 62 degrees. In particular, at the 260 mm mark in the closed ring section the phase was 46 degrees whereas at the 380 mm mark the phase was -16 degrees, producing an overall phase modulation of 62 degrees while transitioning from the closed to the open state of the rings. As shown in Figure 18, we also observed a magnitude variation of -2.7 dB for the same transition.
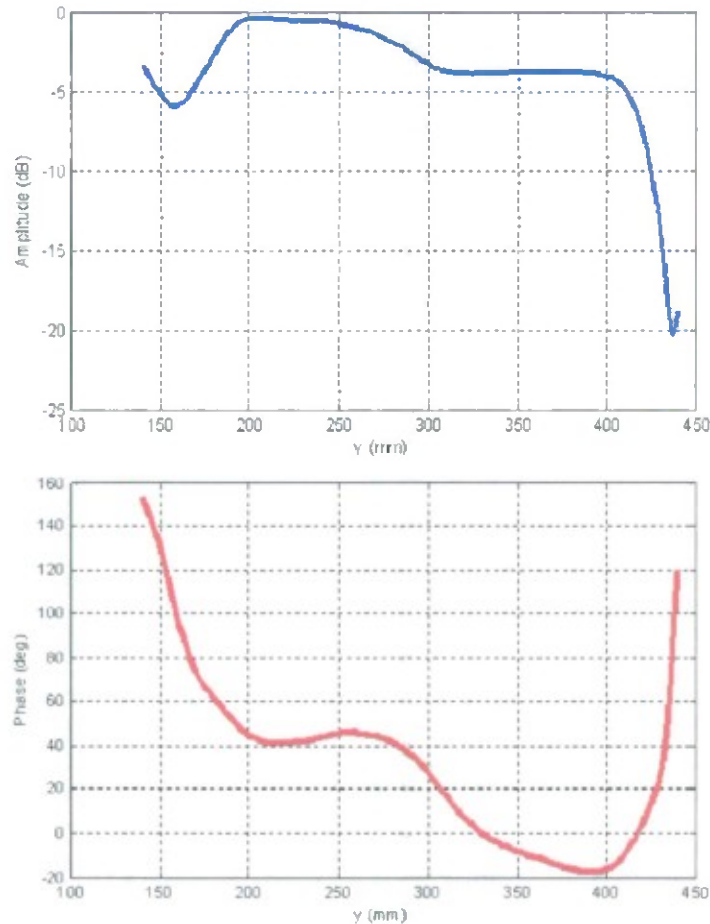
Figure 18. *Scanned data for amplitude and phase variation.*

4.3 Dielectric Input/Out (I/O) Couplers for Waveguide Transition

In order to reduce the insertion loss that may arise from the coaxial feed to the PhC interface due to impedance mismatch, we also designed a coaxial-to-PhC coupler that combines a commercially available coaxial-to-rectangular waveguide transition with a vertically-tapered dielectric line, a horizontally tapered dielectric horn and two vertically-tapered metallic flanges. In our earlier effort we noted that such a taper would improve the coupling to the dielectric medium by reducing the return loss. The height of the dielectric line at its largest point is equal to that of our metal X-band waveguide. Two tapered metallic flanges at the open end of the X-band waveguide were added to contain the out-of-plane radiation from the dielectric horn. The complete I/O coupler is shown in Fig. 2.2, including the coaxial-to-waveguide transition, X-band waveguide, tapered dielectric line and dielectric horn, and the two metallic flanges. The input/output (I/O) couplers provide an efficient means to transfer electromagnetic energy to and from the PhC while producing a small signature.

Figure 19. *I/O coupler*

16

4.4 High Index Contrast (HIC) Self-Collimating Photonic Crystal (SCPhC)

In previous sections, although the propagation loss that was measured for the low-index-contrast (LIC) PhC was considerably lower, the transmission efficiency was not sufficiently high to compete with the established waveguiding mechanisms in the microwave regime. In our current effort we noted that it is easier to achieve self-collimation in HIC PhC since the energy is confined in-plane better within the higher-index material and the out-of-plane scattering is also lower for such a PhC. Thus, there was merit to investigate self-collimation in HIC PhC in order to demonstrate efficient transmission of signal in the microwave frequency. Also, the results achieved for LIC PhCs provided principal insights into self-collimation that allowed us to extend our work to a HIC PhC design.

4.4.1 7.1. Design and Numerical Characterization of HIC SCPhC

The HIC PhC design had a square-lattice structure composed of high index rods embedded in a low-index material. In particular, perforated Eccostock polyurethane foam was used as the low-index material with dielectric constant of 1.073-j0.0023. The material for the rods was ceramics (95% Al_2O_3) whose dielectric constant was 9.1, and a refractive index of 3.01.The physical properties of the ceramic rods are similar to those of the polystyrene material that was used for the LIC PhC; hence, ceramics also offered mechanical strength, and low loss. Given the high refractive index of the ceramic rods we achieved an index contrast ratio of 3:1 between the rods and the perforated foam slab.

In order to design the PhC with the high index rod configuration, we took the following steps. At first, the dispersion diagrams and 2D and 3D EFC were generated using our in-house developed Plane Wave Expansion Method (PWEM) code. TM mode was considered in the design where the electric field would be parallel to the rods. This step provided a guideline about the working frequency and the dimensions of the different parameters used in our design. Following this, a 2D FDTD method, also developed in-house, was employed to simulate the designed PhC in order to obtain the field distribution information within the PhC. Both of these steps are carried out concurrently in order to optimize the EFCs that would provide maximum transmission of signal using the waveguiding technique of self-collimation.
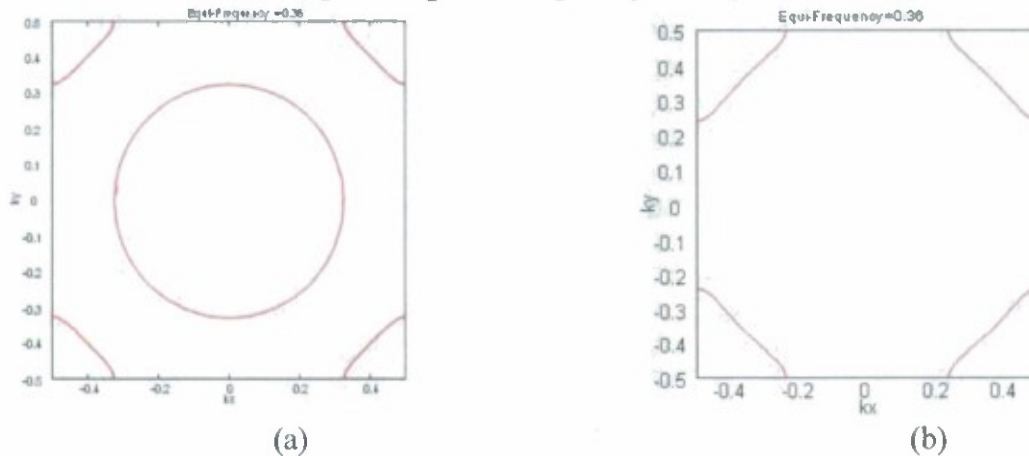

(a)   (b)

Figure 20 *(a) 3D EFC for a = 0.36λ for HIC SCPhC, and (b) equivalent 2D EFC for HIC PhC.*

The design of this HIC PhC presented a particular challenge that we had not faced for the LIC PhC. Since this design used high-index rod, the desired self-collimating behavior is achieved with smaller rods and lattices. Hence, for accurate simulation purposes a denser mesh was needed for small feature size in the design which could eventually increase the computational cost. In order to reduce the complexity of the 3D simulation, a 2D dispersion surface was generated which matched closely to the 3D dispersion surface. This equivalent 2D dispersion diagram is obtained by optimizing the effective refractive index (n_{eff} =1.9) of the 2D PhC. The 3D PWEM simulation of the EFC for $a = 0.36\lambda$, where a is the lattice constant of the PhC, is shown in **Figure 20**(a). The matched 2D EFC is shown in **Figure 20**((b).

17

2D FDTD simulation was carried out to optimize the dimensions of the lattice of the HIC PhC. In this manner we were able to design a nearly square EFC for the first band of this PhC such that the group velocities having the same direction, perpendicular to a straight side of the square EFC would be incident upon a larger spatial angle for self-collimation. From the given EFC we anticipated that there would be self-collimation for a normalized frequency, $\omega_n = 0.36$, that is, for $a = 0.36\lambda$ for a TM mode configuration. It is important to note that the dielectric constant varies slightly with frequency; hence, the values given for the dielectric constant of our materials were calculated at our frequency of operation, which for this PhC is 10.1GHz. At this frequency the wavelength of the light is λ_0 =30mm. The height of the rods was optimized to obtain a flat dispersion surface for self-collimation. We found the ideal height $h = a$ corresponding to 10.6 mm, and the diameter of the ceramic rods of $d = 0.6a$ corresponding to 6.35 mm. Since the first band at the selected frequency is 45°off-angle to the lattice orientation, we rotate the PhC lattice by 45° for our simulations and experiments.

4.4.2   Numerical Simulation of HIC SCPhC

As mentioned before, we employed a 2D FDTD algorithm for simulation purposes. In this section we present an overview of the numerical simulation and results for the HIC SCPhC.

A schematic of the setup is shown in **Figure 21**, which shows the two I/O couplers and the HIC PhC. The designed SCPhC was excited with a Gaussian beam whose beamwidth was half the width of the waveguide. The input beam would travel through PhC via self-collimation and finally propagated field would be captured at the output of the PhC through via a detector.
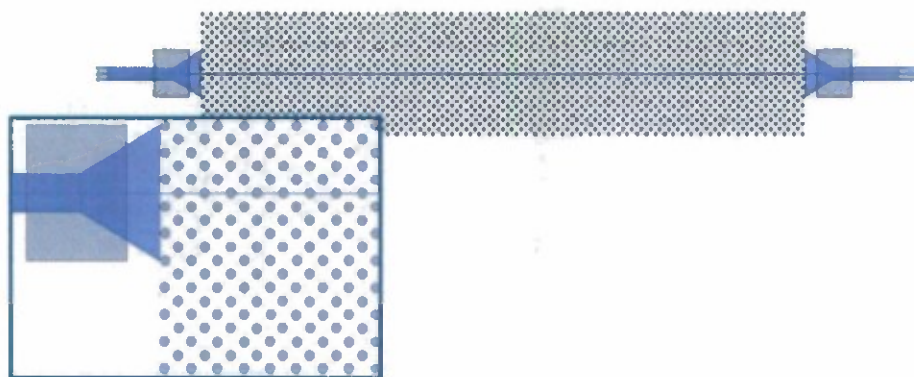
Figure 21 *Schematic for HIC PhC simulation setup*
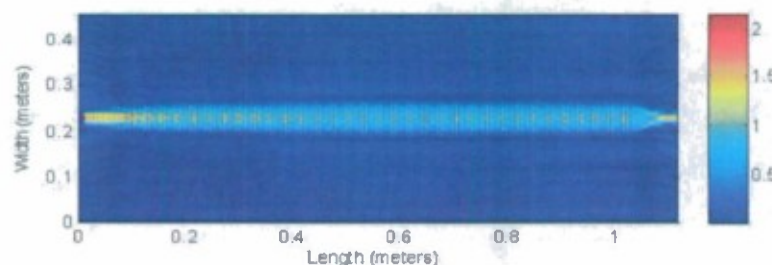
Figure 22. *FDTD simulation of electric field distribution for HIC PhC at 10.1 GHz.*

Based on the setup shown in **Figure 21**, we simulated a 1m long HIC PhC as shown in **Figure 22**. The simulation displays the electric field (E_z) distribution. The self-collimation noted in the simulation result verified our designed HIC with $a = 0.36\lambda$ at a frequency of 10.1 GHz. Furthermore, using the field components E_z and H_y, the calculated transmission power loss was 0.4 dB/m or 0.011 dB/λ as shown in Fig. 3.4. It is important to note that since this simulation is two-dimensional, it does not contain any

18

information about the height of the PhC so these results do not account for the out-of-plane scattering loss.
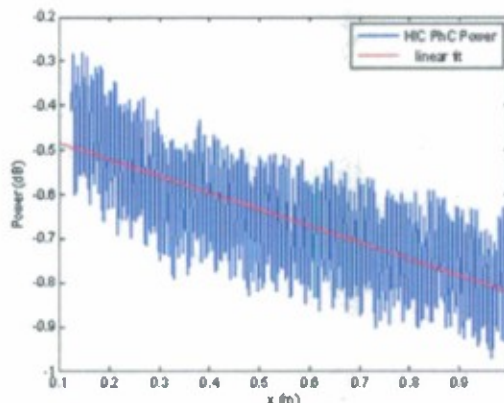

Figure 23 *Power distribution along the 1m long HIC PhC at 10.1 GHz.*

4.5   Fabrieation of HIC SCPhC

Given the encouraging numerical result, we fabricated the HIC PhCs in order to verify it with experimental measurements. Based on the simulated parameters, we fabricated the PhC using a Computer Numerical Control (CNC) router to drill the periodic lattice of cylindrical holes with a diameter $d = 6.35$ mm and lattice constant $a = 10.6$ mm on the Eccostock polyurethane foam slab. The design of the PhC was tuned to the appropriate frequency to accommodate the diameter of the ceramics rods that were available from the manufacturer. Since ceramics are higher-index materials, they are also denser and mechanically harder than the polystyrene material used for the LIC PhC. Thus, cutting and machining ceramics required very advanced macro-machining tools, such as the grinders and water-jet cutters. The ceramic rods were cut to the desired height of 10.6 mm. Subsequently, we used these rods to fill the periodically drilled holes in the polyurethane foam slab. A picture of the rods and the complete PhC is shown in Fig. 4.1.
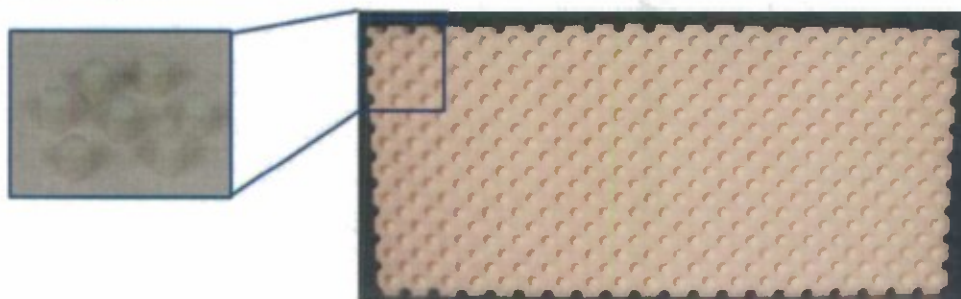

Figure 24 *Fabricated HIC PhC.*

4.6   Experimental Demonstration of Self-Collimation in HIC and LIC PhC

Side View | **Top View**
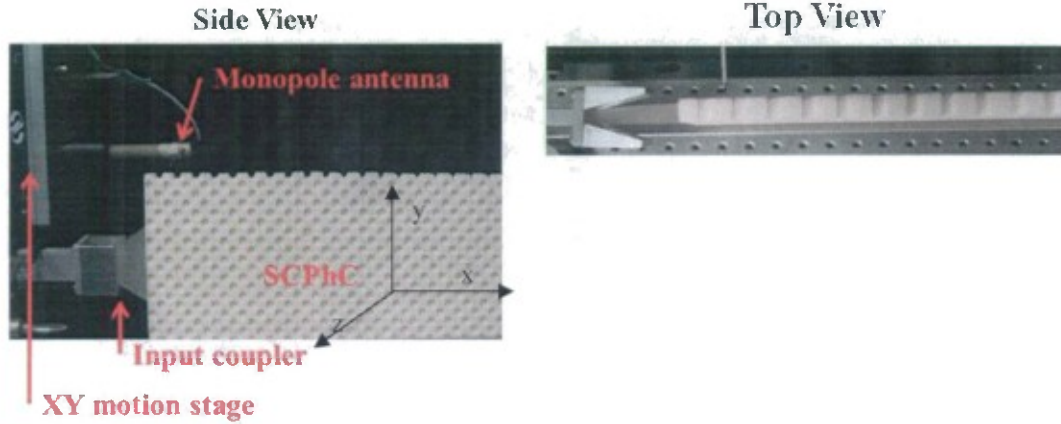
Figure 25 *Experimental setup for 2D scanning of SCPhC.*

In order to verify the self-collimating behavior of the PhC experimentally, we setup a near-field scanning system which included an Agilent 8722B network analyzer, a motion control system, and an S-parameter measurement system. In our setup, the sample was placed next to the detector with a dielectric I/O coupler as the input source as seen in Figure 25. We chose a 1mm monopole antenna as the detector that captured signal and output it back into port 2 of the network analyzer. The field distribution within the PhC was acquired by scanning the surface of the PhCs which would detect the evanescent waves of the propagating field in the slab. We left a gap of approximately 5mm between the detector and the surface of the PhC and we assumed that the evanescent wave distribution is proportional to the field inside the PhCs. The input signal was fed into the PhC with the dielectric I/O coupler that was positioned at the edge of the PhC. The E_z component of the electric field was perpendicular to the PhC slab to coincide with the detecting monopole antenna whose tip was perpendicular to the surface of the PhC slab. We set the frequency of the feed signal at 10.1 GHz and scanned the slab with a step size of 1.5 mm in both x and y axes. We also developed a custom Labview program to synchronize the motion of the 2D scanning system and for the measurement of the signals in the network analyzer.

(a)   (b)
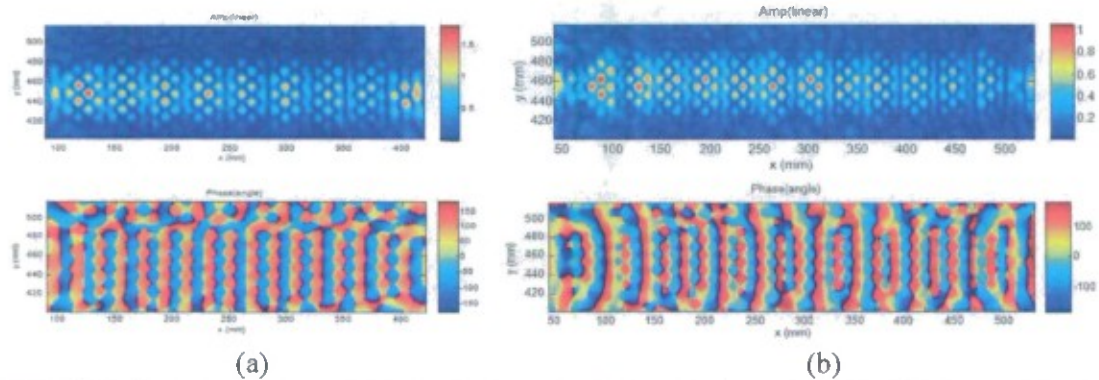
Figure 26. *Measured electric field distribution (amplitude and phase) for HIC PhC for (a) 12" slab, and (b) 18" slab.*

Figure 26 (a and b) shows the experimental results for amplitude and phase of the field distribution inside a 12-inches and an 18-inches HIC PhC, respectively. The distribution of the electric field component E_z, both in amplitude and phase, shows that the propagation is only along one direction through the center line of the picture and the microwave signal is indeed self-collimated through the HIC PhC. For comparison, we also carried out similar scanning measurement for the LIC PhC as shown in **Figure 27**(a, b) for amplitude and phase of the electric field. The amplitude and phase shows that the propagation is only along one direction through the center line of the picture. However, when comparing

20

Figure 26(a) and Figure 27(a), qualitatively it can be seen that the confinement of the wave can be considered superior in the HIC PhC. Thus, to have a quantitative measure we carried out a through transmission analysis as presented in the next section.
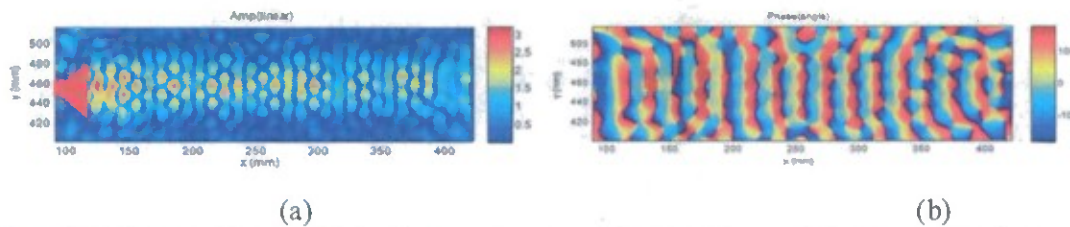

(a)   (b)

Figure 27 *Measured electric field distribution for a 12-inch LIC PhC (a) amplitude, and (b) phase*

4.6.1   Experimental Verification of Transmission Efficiency in HIC and LIC SCPhC

In order to carry out transmission measurements for the PhCs, we setup a microwave measurement system that included an Agilent 8722B network analyzer, two sets of 3.5 mm coaxial cables, two I/O couplers and the LIC/HIC PhCs. Figure 5.4(a) shows a setup where a PhC is placed in between the input and output coupler for transmission measurements. The setup was calibrated using the standard SLOT (Short, Load, Open, Transmission) calibration. For the experimental measurement of the insertion loss through the I/O couplers and the SCPhC, first we connected port 1 of the network analyzer using a 3.5 mm coaxial cable to the coaxial-metal waveguide transition of the input coupler. This coupler fed the input signal to the PhC through the I/O coupler, which was essentially a dielectric tapered transition waveguide. The coupler was fused to the first row of rods of the PhC to have a seamless transition between the coupler and the PhC at the interface. Similarly, the output coupler was connected at the other end of the PhC to couple the beam propagated through the SCPhC to the second port of the network analyzer. Using this experimental setup, at first, we measured the transmission through a 12" HIC at a frequency of 10.1 GHz by capturing the S-parameters in the VNA. The measured insertion loss was -1.61 dB as shown in Fig. 5.4(b) in red curve for the HIC PhC. Following this, we measured the transmission for an 11.5" LIC PhC measured at 12.1 GHz. The insertion loss was -2.45 dB as shown by the blue curve in Fig. 5.4 (b). This measurement showed that the transmission in HIC PhC was 0.84 dB higher compared to the LIC PhC measured under the same conditions. The two kinds of PhCs could not be compared at the same frequency because of fabrication constraints. In particular, the LIC PhC was designed to operate at 12.1 GHz based on the diameter of Rexolite rods that were available from the manufacturer, but for the dimensions of the available ceramic rods that suited our HIC design, the closest frequency of operation was 10.1 GHz. Despite this slight variation, the frequencies were close enough that a comparison of the transmission through the two PhC structures was acceptable as the stated purpose of our effort was to fabricate a SCPhC waveguide in the microwave regime, particularly in the X-band (8 – 12 GHz). This experiment further justified our observation about superior self-collimation in HIC PhC that was made
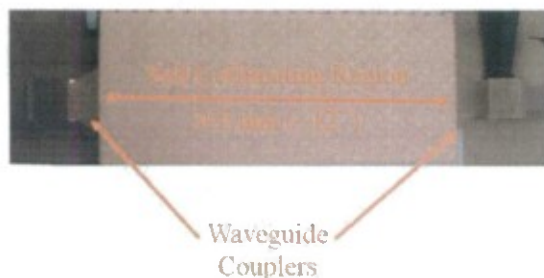

Figure 28 *(a) Setup for transmission measurements for the PhCs*
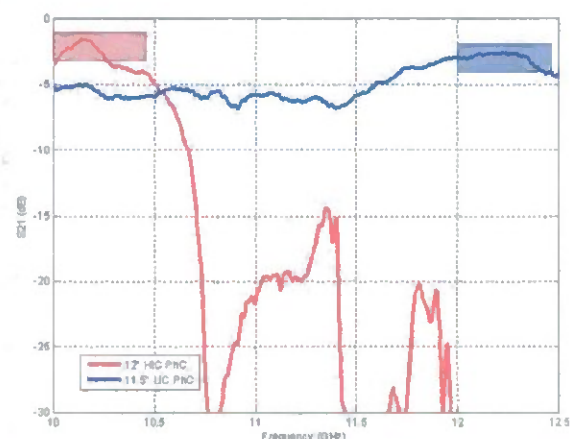
21

Figure 29 *(b) Transmission measurements of HIC and LIC PhCs*

based on the near-field scanning result.

To further explore the different contributing factors responsible for the transmission loss, we set out to isolate the coupling and transmission loss components in our integrated SCPhC system. We define the coupling loss, L_c (marked as 1 in Figure 30) as the component of the insertion loss caused by the transition, through the I/O couplers, from the coaxial medium to the SCPhC. In a similar manner, we define the transmission loss, L_t (marked as 2 in Figure 30) as the component of the insertion loss that results from the in- plane divergence of waves in the SCPhC.
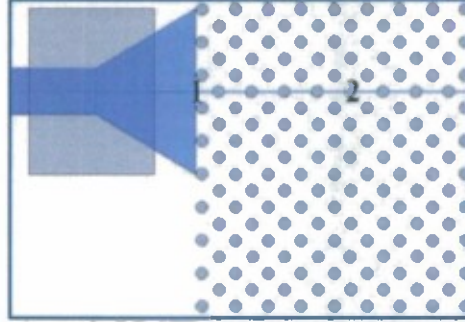

Figure 30 *Transmission loss components in the SCPhC system.*

The steps for calculating the (L_c) and (L_t) required taking measurements of the insertion loss of the PhC of different lengths in order to back out the coupling loss(L_c) that existed between the PhC and the coupler. Thus, with the knowledge of the coupling loss, the transmission loss (L_t) can be calculated by subtracting the (L_c) from the total insertion loss.

In order to isolate the loss components for both the LIC and HIC PhCs, we first fabricated two more LIC PhC slabs of lengths 9.1" and 16.6". Exploiting the flexibility and homogeneity of our SCPhC design, which allowed us to feed a signal arbitrarily along the width or length of the slab, we were able to measure the insertion loss for five different lengths: 5", 11.5", 12.5", 14", 16.5". We experimentally measured the insertion loss for the five different PhCs, obtaining the results presented in Figure 31. The measured insertion loss is also tabulated in Table. 1. These measurements yielded a good agreement with the numerical results for the same PhC lengths.

Following this, using the results shown in Figure 31, we picked the data point at 12.1 GHz for each PhC length and plotted the data for the insertion loss as shown in Figure 31(a). This result allowed us to compute the coupling loss component by extending the line of the insertion loss to the y intercept, which essentially gave us the coupling loss between the PhC and the coupler. This also made it simple to determine the transmission loss component of the photonic crystal by simply subtracting the total coupling loss component from the insertion loss for the complete system. As an example, the total transmission loss for the 11.5" LIC PhC slab was measured as -2.45 dB, and the coupling loss calculated from the y-axis intercept was -0.6 dB (Figure 31(a)), which gave us a transmission loss of (L_t) of 1.85 dB for the 11.6" PhC. Accordingly, we calculated the transmission loss component per unit length for the LIC PhC as $L_t = -0.17\pm0.01$ dB/λ or 0.17 ± 0.01 dB/inch at 12.1 GHz.
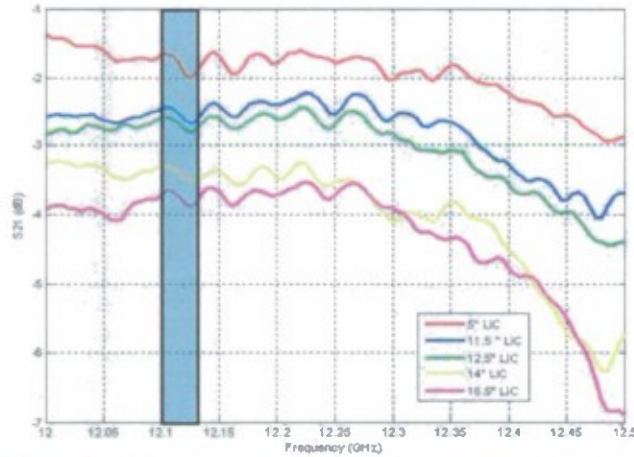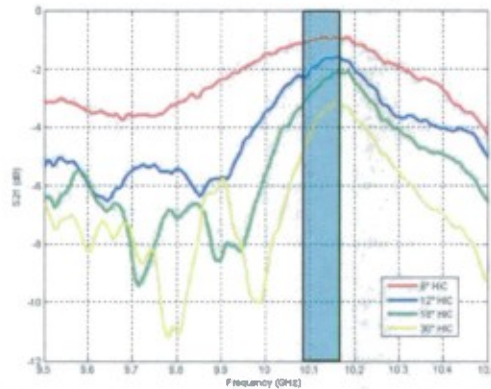

Figure 31. *Measured transmission loss for different length of slabs for LIC PhC.*

22

(a)   (b)
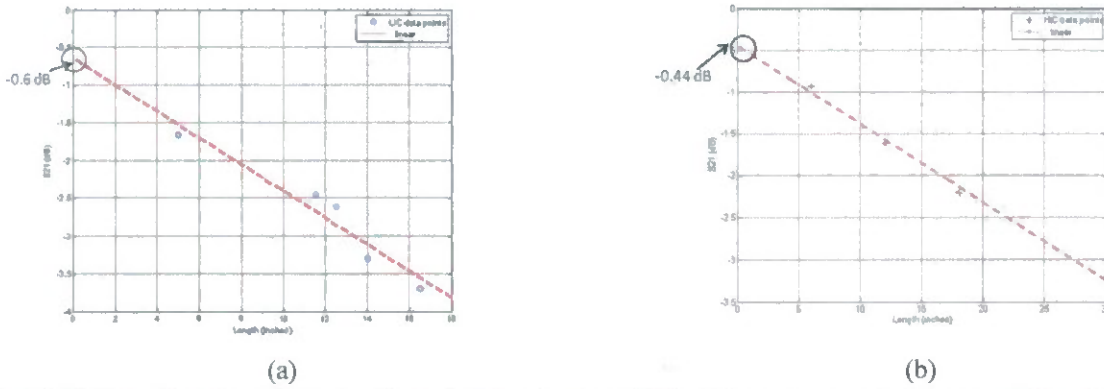
Figure 32 *Coupling loss calculation through linear extrapolation of the transmission data for different length of PhCs, (a) LIC PhC, and (b) HIC PhC.*

Similar to our previous experiment for the LIC PhC, we performed transmission measurements for the HIC PhC in order to determine and isolate the transmission loss components of the insertion loss in our integrated SCPhC system. Thus to collect enough S-parameter data points to calculate the coupling loss, we further fabricated an 18-inch HIC PhC slab to measure the insertion loss for four different lengths, 6", 12", 18" and 30" by putting together the slabs in different arrangements. We experimentally measured the insertion loss for the four different PhCs, as shown in **Figure 33**.

Figure 33 *Measured transmission loss for different length of HIC PhCs.*

Similar to the LIC measurements, using the results shown in **Figure 33**, we picked the data point at 10.1 GHz for each PhC length and plotted a single line for the insertion loss for PhCs of different lengths as shown in Figure 32(b). This result allowed us to compute the coupling loss (L_c) component which was 0.44 dB. Thus, the transmission loss (L_t) was 1.17 dB for the 12" HIC PhC with the total insertion loss of -1.161 dB. From this data we further calculated the transmission loss component of the HIC PhC per unit length as L_t = -0.09±0.005 dB/λ, or -0.08±0.005 dB/inch, Thus, L_t = -3.14±0.2 dB/m at 10.1 GHz. Based on the above numbers for the transmission loss (L_t), we can conclude that there is an improvement in transmission by a factor of 2 for the HIC PhC when compared to the LIC PhC. The improvement can be accounted for the higher refractive index rods that were used for the HIC PhC which provided better in-plane confinement of the field leading to a lower out-of-plane scattering Thus, the results also confirm our observations made from the near-field scanning result.

23

Table 1. Measured transmission data for HIC and LIC PhC slabs

LIC PhC Length (inches)	Transmission (dB) 12.1 GHz	HIC PhC Length (inches)	Transmission (dB) 10.1 GHz
5	-1.66	6	-0.93
12.5	-2.61	12	-1.61
14	-3.3	18	-2.2
16.5	-3.69	30	-3.2

4.7 The 'Fishnet' Metamaterial

The 'fishnet' metamaterial structure, as depicted in Fig. 1, comprises a pair of metallic thin films with a periodic array of rectangular perforations (or 'holes') separated by a dielectric filler layer. Such devices have been investigated in recent years to explore 'left-handed' behavior in the mid-IR and near-IR regions [1, 2]. The metal-dielectric-metal strips parallel to the magnetic field form an LC circuit whereby the anti-parallel currents induced in the metal layers straddling the dielectric layers (by the magnetic field of the incident optical signal) lead to the formation of a magnetic field which counteracts that of the incoming optical signal [1, 2]. This brings about a negative permeability around a resonance. On the other hand, the wires parallel to the electric field are essentially dilute Drude metals below their effective plasma frequency which bring about negative permittivity [1, 2]. For frequencies where both permittivity and permeability are simultaneously negative, the refractive index also becomes negative [1, 2].
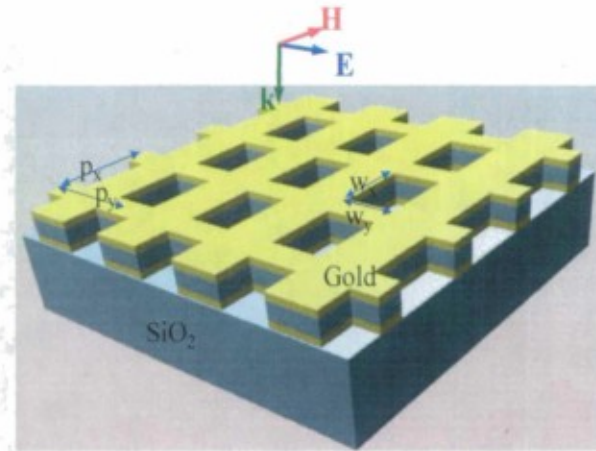

Figure 34 *A schematic of a 3D "fishnet" structure.*

4.7.1 The 'Fishnet' Metamaterial

The aim of this work was to achieve negative refraction at an operational wavelength of 1500nm. To this end, rigorous FDTD modeling was utilized to determine the dimensional attributes of a 'fishnet' metamaterial which exhibits negative constitutive parameters around 1500nm. The dimensional attributes of the resultant structure, in terms of the nomenclature established in **Figure 34**, comprised rectangular 'holes' with $w_x = 400$nm and $w_y = 280$nm arrayed at periodicities $p_x = p_y = 650$nm. The metallic layers consist of 30nm thick Au thin films. The dielectric spacer is a 60nm thick SiO_2 layer.

4.7.2 Fabrication Process

Figure 35 outlines the steps for the fabrication process developed to realize the simulated 'fishnet' structure configuration. As depicted in steps 1 and 2 of **Figure 35**, this process starts with a deposition of a thick (350nm) layer of Si on top of a quartz substrate using a PECVD tool followed by an e-beam evaporator deposition of a thin (50nm) Cr layer.

24
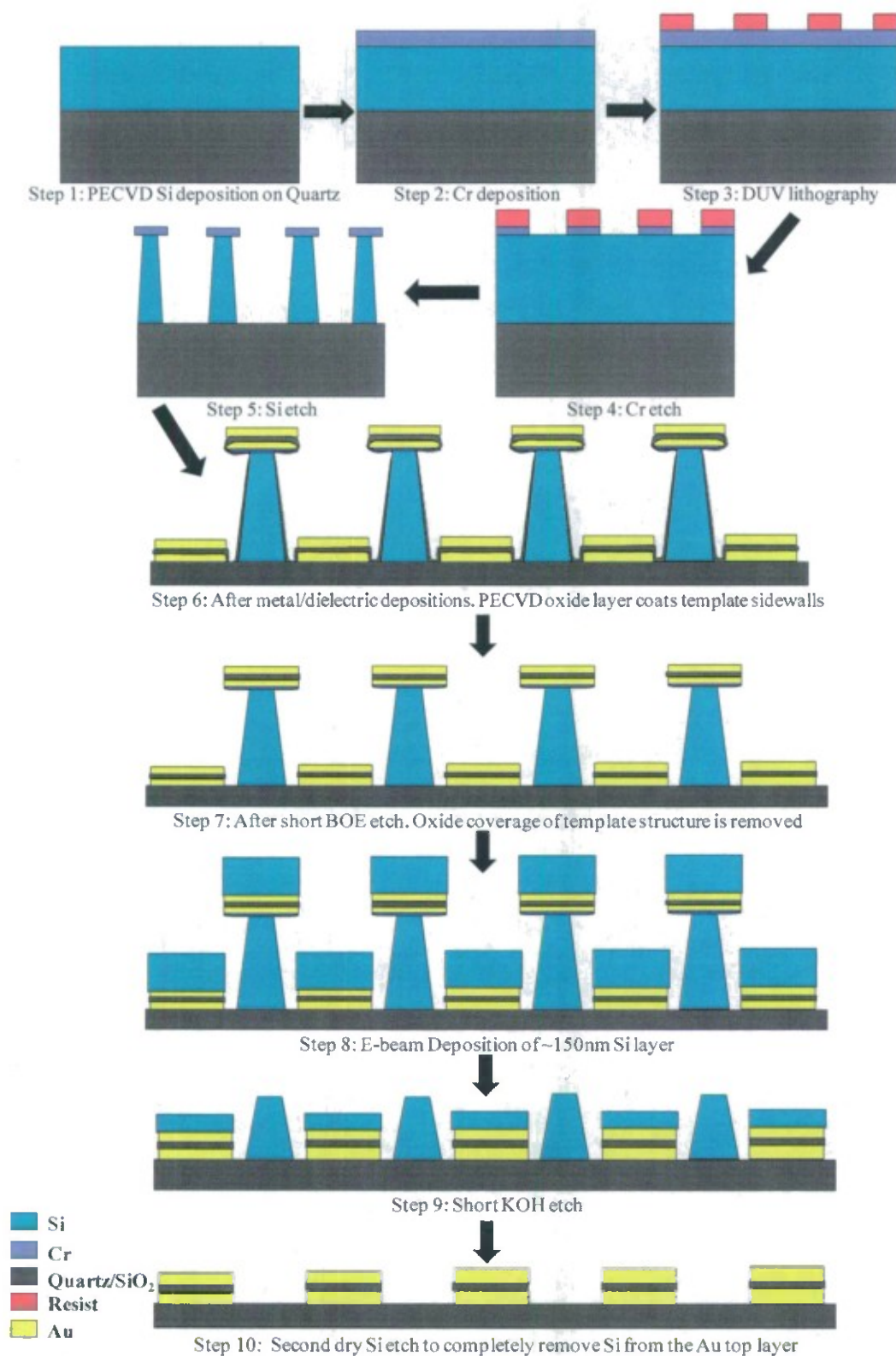
Figure 35 The fabrication process.

In step 3, a layer of SU-8 resist (~200 nm thick) is spin-coated onto the above described substrate and exposed to DUV (220 nm) radiation in a mask aligner using a dark-field exposure mask with rectangular

holes corresponding to the 'fishnet' structure as described in the previous section. The mask aligner is fitted with a set of filters to remove long-wavelength components from the UV source. Additionally, an optical filter with a transmission window of 30 nm around 220 nm is directly placed over the exposure mask with the SU-8 coated sample substrate placed against it in 'hard' contact. Elimination of longer UV wavelengths is essential to prevent diffracted radiation from crosslinking the resist layer in undesired areas. Calibrating the UV exposure dose is also necessary since SU-8 resist is highly absorptive at DUV wavelengths. A lower than optimal exposure dose will prevent the exposed patterns from anchoring down to the substrate whereby they will be removed during development. On the other hand, prolonged exposure will lead to some of the diffracted long wavelength components to exceed the threshold exposure dose resulting in crosslinked resist in undesired areas. After exposure, the samples are reverse baked and developed to yield the complimentary template structure comprising resist islands corresponding to the holes in the 'fishnet' structure.

In step 4, chlorine chemistry is utilized in an Inductively Coupled Plasma (ICP) tool to etch the Cr layer with the SU-8 pattern developed in step 3 as the etch mask. Details of this dry etch process is provided in Table 1. Cl_2, O_2 and Ar are the gasses which are used for the above. The etch rate is approximately 60nm/sec. The use of a high amount of Ar gas in the recipe renders it a physical etch process to a certain extent. Thus, the SU-8 soft mask pattern formed earlier is completely removed at the conclusion of the Cr etch step. The resultant patterned Cr layer forms the etch mask in step 5 where another dry etch process is used to etch through the underlying PECVD deposited Si layer to form the sacrificial template structure. The sacrificial template corresponds to the holes in the 'fishnet' structure.

Gasses	ICP Power (W)	Bias Power (W)	Pressure (Pa)
Cl_2(25 sccm), Ar (20 sccm) O_2(20 sccm)	275	30	0.7

Table 1. Dry etch recipe to form the Cr etch mask for the Si template structure.

The ICP etch process used for etching the Si layer is based on the Bosch process [3]. The details of the dry-etch process loop that was implemented to achieve the sacrificial template structure is provided in Table 2. This etching method involves repeated implementation of a process loop comprising short etching and passivation steps. The etching steps are highly isotropic and use SF_6 gas. The passivation steps use C4F8 gas for polymer deposition on the etched sidewalls. The duration of the passivation and etching phases in the process loop can be tuned to precisely control the anisotropy and etch-rate of the process. Thus, it allows for the formation of template pillars, at the conclusion of step 5, with a mushroom-shaped cross section profile. This is beneficial for successfully carrying out a 'lift-off' process. The Cr etch-mask used for the Si etching step affords etch selectivity of well over 100:1.

26

Gasses	ICP Power (W)	Bias Power (W)	Pressure (Pa)
Passivation Step			
C_4F_8 (20 sccm)	450	15	4
Etching Step			
SF_6 (25 sccm)	500	5	0.75

Table 2. Dry etch recipe to form the Si template structure with Cr etch mask. The selectivity of this process is greater than 100:1.

After forming the sacrificial template structure, Au-SiO$_2$-Au layers are deposited, as shown in step 6. An e-beam evaporator has been used for deposition of Au. The oxide layer has been deposited in a plasma enhanced chemical vapor deposition (PECVD) tool. The thicknesses of the Au and the oxide layers are approximately 30 nm and 60 nm respectively, in agreement with our simulation results. 5 nm Cr layers are deposited at the quartz/Au and oxide/Au interfaces to mitigate the poor adhesion properties of Au. It is important to note that since oxide deposition is carried out using the highly isotropic PECVD process, the template sidewalls incur oxide coverage, as depicted in step 6 of Fig. 2. In order to facilitate the final removal of the Si sacrificial template it is crucial to remove this oxide coverage. This is accomplished with the short BOE etch (~5 seconds) in step 7. The sandwiched oxide layer is protected during this step by the Au layers straddling it. However, this oxide layer, along with the Au layer lying above it, can be removed if the etch time is prolonged.

After step 7, one could proceed to remove the Si template pillar structure with a wet etch process using KOH. However, when this was attempted, the entire sample structure would be littered with Au-SiO$_2$-Au discs removed from the top of the template structure. This is due to the tendency of Au nano-particles to aggregate and to cling on to metallic surfaces [4]. This can be avoided to a certain extent by performing the final KOH etch process within a sonication bath. However, the need for maintaining the KOH solution at an elevated temperature can pose problems with regards to this approach. Steps 8 and 9 were incorporated in the fabrication process to address the issue of Au aggregation.

In step 8, a thick (~150 nm) Si layer is deposited in an e-beam evaporator. The 'line of sight' e-beam deposition process ensures that this Si layer does not coat the template sidewalls. The thickness of this Si layer deposited has to be thicker than the width of the Si-template pillars at their narrowest point (~100 nm, near the top of the pillars). In step 9 a short (~8 seconds) wet etch with 20% KOH at 60°C is conducted. This etch duration is calibrated to be long enough to etch through the thinnest portion of the template pillars while ensuring that a part of the e-beam deposited Si layer (Step 8, Fig. 2) survives at the base of the pillar structure and shields the top-surface of the 'fishnet' structure (Step 9, Fig. 2).

Step 9 is carried out successfully because of three reasons. Firstly, as mentioned above, the Si layer deposited in step 8 is thicker than the width of the template pillars at their narrowest point. Thus, a short KOH etch ensures that a layer of the e-beam deposited Si survives even as the template pillars are removed. Secondly, the isotropic KOH etch process attacks the template structure from every direction, as opposed to e-beam deposited Si layer at the base of the templates which is etched only from a top-down direction. This ensures that the template pillars are etched at a faster rate. Thirdly, the e-beam evaporator deposited Si layer is denser as compared to the PECVD deposited Si layer used to pattern the sacrificial template structure. This also results in a higher etch rate of the PECVD deposited Si layer. Thus, after Step 9 of the fabrication process, a Si layer of ~50 nm survives and shields the metallic top-surface of the 'fishnet' structure. This significantly reduces the re-deposition of Au-SiO$_2$-Au discs removed from the top of the template pillars. Any remaining Au-SiO$_2$-Au discs adhering to the device structure are easily removed by wiping the samples gently with laboratory wipes. The Si Layer coating the sample to-surface prevents the device structures from being scratched when the samples are wiped with laboratory wipes.

27

The fabrication process is concluded in Step 10 when a dry etching step is used to remove the remaining Si layer coverage from the top of the device structure. The underlying Au and oxide layers remains unaffected by the Si dry etch.

4.7.3   Fabrication Results

Fig. 3(a) is an SEM image of a sample after the dry etching steps which form the template structure (Steps 4 and 5 of Fig. 2). The mushroom-like profile of the etched 'pillars', apparent from Fig. 3(a), is beneficial towards implementing a 'lift-off' process. Fig. 3(b) shows a sample after deposition of the Au-SiO_2-Au layers (Step 6, Fig. 2). One can observe that the widths of the pillars at their narrowest points are approximately 200nm. In comparison, in Fig. 3(c), which depicts a sample after the short BOE etch (Step 7 of Fig. 2), one can observe that at their narrowest point the width of the pillars are only about 100nm. This indicates a successful removal of the oxide coverage from the Si template side-walls after the brief BOE etch.

(a)

(b)

(c)
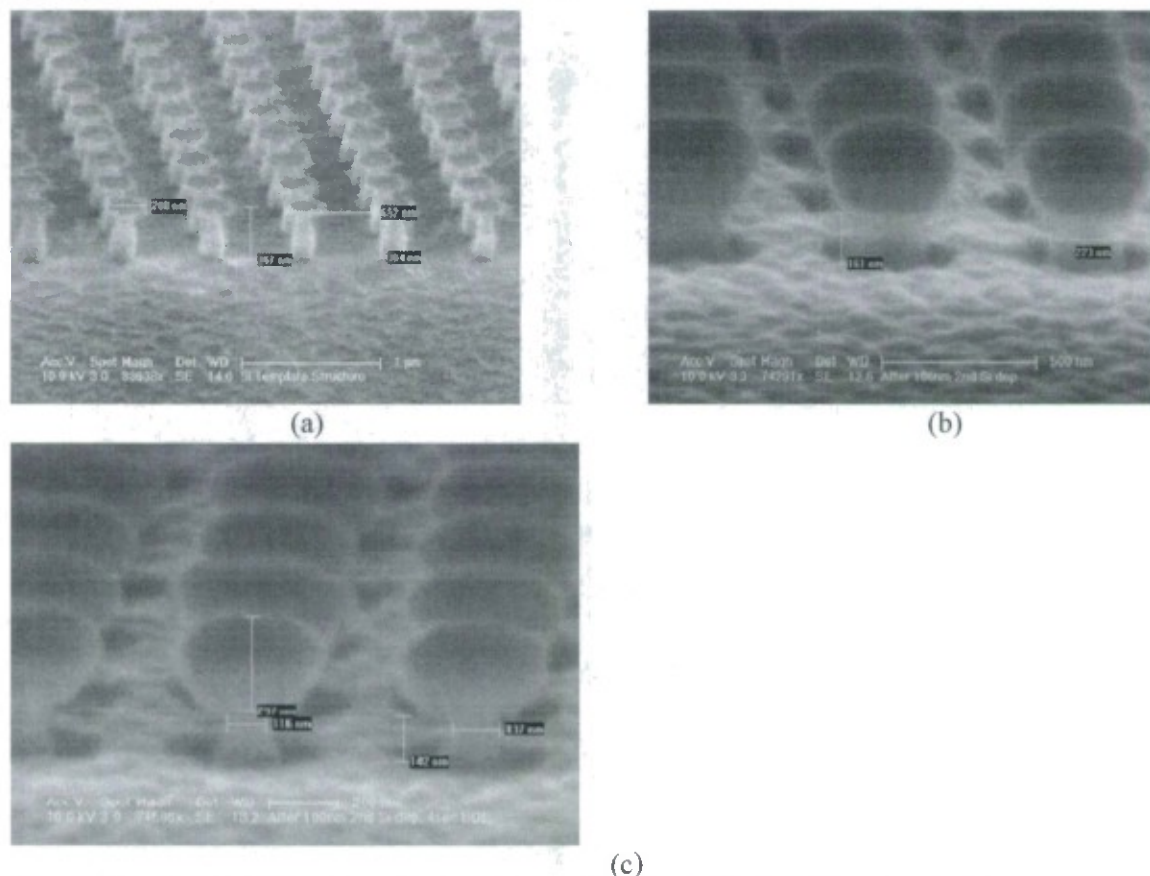
Figure 36 (a) The template pillars after dry etching. (b) Sample after deposition of Au-oxide-Au layers. (c) Sample after ~7second BOE etch.

Figure 37(a) depicts a sample after the KOH wet etch was used to remove the template structure right after Step 7 of Fig. 2. One can observe Au-SiO_2-Au discs, which were atop the template structure prior to the KOH etching step, adhering to the sample structure. This is due to the tendency of Au nano-particles to aggregate with each other and to cling on to metallic surfaces as discussed earlier [4].

28

(a)

(b)

(c)
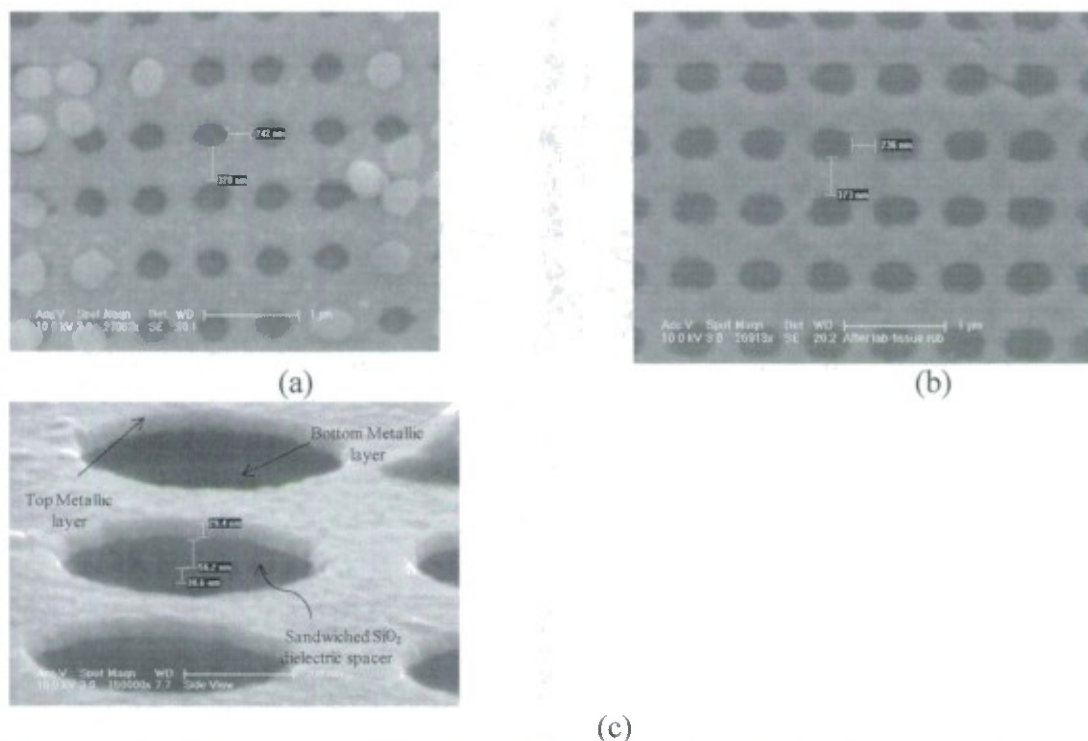
Figure 37*(a) Top-view of a fabricated device with Au-SiO₂-Au discs re-deposited on to device structure. (b) Top-view of a fabricated device after Step 9 of fabrication process. (c) Side-view of a fabricated device.*

In order to avoid the Au aggregation problems, Steps 8 and 9 were added to the fabrication process as described in the previous sections. Fig. 13(b) depicts a sample after step 9. One can clearly observe that the sample is devoid of any Au-oxide-Au discs that could be seen in Fig. 13(a). A very high degree of uniformity is also apparent. Fig. 13(c) depicts a side-view of a sample after the final step of the fabrication process. One can observe the top and the bottom Au metallic layers, each about 30nm thick, with the SiO_2 dielectric layer, about 60nm thick, sandwiched in between.

The 'holes' of the fabricated 'fishnet' structure, as depicted in Fig. 4(b), are somewhat oval as opposed to the rectangular shape that the simulation results require. This can be attributed to diffraction effects during the deep-UV lithography process to define the complimentary template structure, since the exposure wavelength (220nm) and the 'hole' dimensions are very close to each other. Diffraction effects also bring about a slight disparity between the dimensions of the 'holes' in the fabricated 'fishnet' structure and those required by the simulation results. This can lead to slight shifts of the resonant frequency as compared to the simulation results.

A number of steps can be implemented to mitigate these lithography related discrepancies. Firstly, thinning the SU-8 resist layer further during the lithography step performed on top of the Cr layer (Step 1, Fig. 2) will reduce the required deep-UV exposure dose. This will prevent the long wave components in the UV exposure source from exceeding threshold dosage which will in turn obviate resist crosslinking in undesired locations. Secondly, fabrication discrepancies due to lithography can also be minimized by more effective removal of long wave components from the exposure source.

The advantages presented by this fabrication process are very significant. For instance, this fabrication process is ideally suited for fabrication of these devices over very large areas in any arbitrary shape (in the plane of the substrate), predicated by the size and design of the exposure mask used for defining the template structure. Also, all of the fabrication techniques utilized in this process are compatible with the prevalent semiconductor processing technology available at the present. Thus, this fabrication process renders these devices mass producible. This fabrication process also allows for deposition of multiple

stacks of metal-dielectric-metal layers whereby the fabricated devices can be rendered three dimensional which will enhance the 'left-handed' properties and facilitate direct demonstration of these properties.

4.7.4   Dual-Beam Michelson Interferometer Characterization set-up

In order to accurately obtain the optical parameters of the fabricated devices, the complex transmission (t) and reflection (r) coefficients have been measured using a novel Dual-beam Michelson interferometry approach illustrated in Figure 38 and Figure 39. Interferometric approaches, especially for measuring the phase components of the t and r, require invariance in the characterization setup. This necessitates high end optical and translational components. The characterization process presented here allows for simultaneous characterization of the MM and relevant reference media during r and t measurements. Thus, the characterization set-up is identical during t and r measurements for the MM and reference media. This results in accurate and repeatable phase measurements and obviates high end optical and translational elements. Furthermore, concurrent measurement of the MM and reference media significantly speeds up the characterization process.

The characterization setup comprises a calcite beam displacer (CBD) which splits a collimated 1mm diameter 45° linearly polarized tunable laser output into 90° and 0° polarized beams, depicted as the blue and red optical paths in Figure 38 and Figure 39. The parallel 0° and 90° linearly polarized beams from the CBD are then split into the Arm 1 and Arm 2 beams using a beam splitter. In Arm 1, either of the linearly polarized beams emanating from the CBD can serve as the MM beam. However, since the 'fishnet' structure is polarization dependent, it must be ensured that the MM beam is polarized parallel to the thinner 'wires' of the fabricated structure as shown in the inset of Figure 38. Also, it must be noted that the CBD is shown in Figure 38 and Figure 39 to be splitting the tunable laser signal horizontally for convenience of illustration. In reality the beam displacer is used so as to split the tunable laser beam vertically. This minimized the disparity in geometric path length between the reference and MM beams.

For t measurements a layer of air of the same thickness as the MM is considered as the reference medium for t measurements. This is facilitated by having the reference beam pass through a blank portion of the quartz substrate adjoining the MM structure during t measurements. Furthermore, since both MM and reference beams pass through the host quartz substrate, there is no phase disparity between them other than what the MM brings about. The configuration of the measurement set-up for t measurements is illustrated in Figure 38.
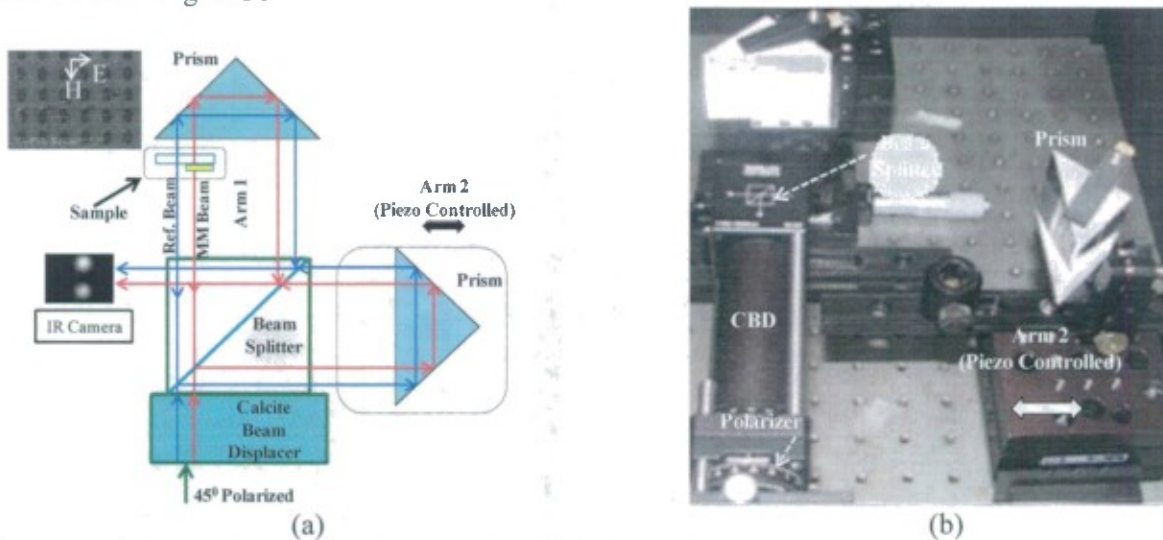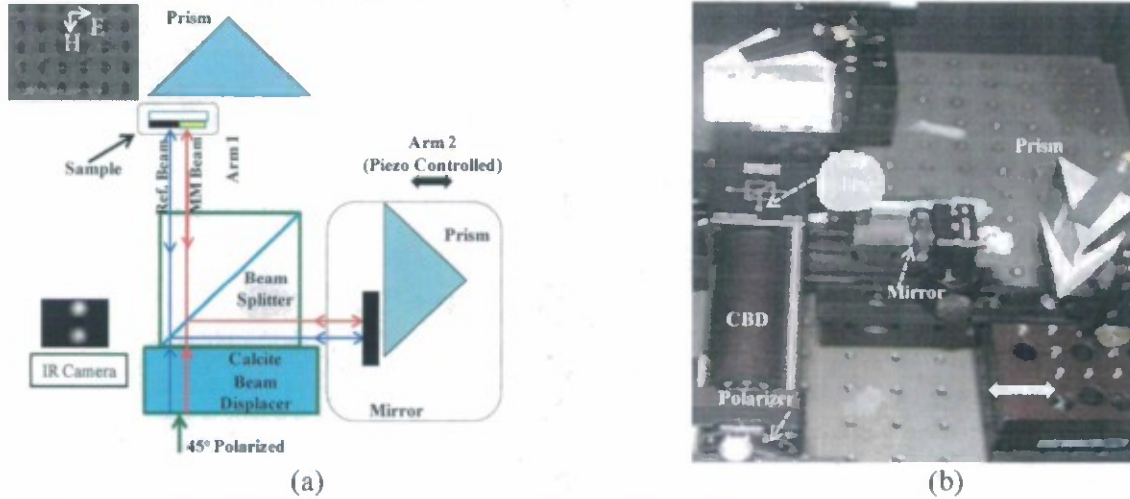

Figure 38 *(a) Measurement set-up for t. (b) Picture of t measurement set-up.*

For r measurements, a flip-mirror is placed before the right angled prism in Arm 2. The gold film adjoining the MM is used as the reference surface. The flip mirror in the reference arm has a known reflectivity, which normalizes the gold film. The configuration of the measurement set-up for r measurements is depicted in Figure 39.

Figure 39 *(a) Measurement set-up for t. (b) Picture of t measurement set-up.*

The measurement process during the t and r data acquisition involves changing the reference arm length by ~50nm increments and scanning the near-IR wavelength range of interest, i.e., 1300-1600nm, for each of these increments. The intensities of the recombined (from the Arm 1 and Arm 2) MM and reference beams are recorded for every scanned wavelength after every change of the Arm 2 length using an IR camera, as shown in Figure 38 and Figure 39.
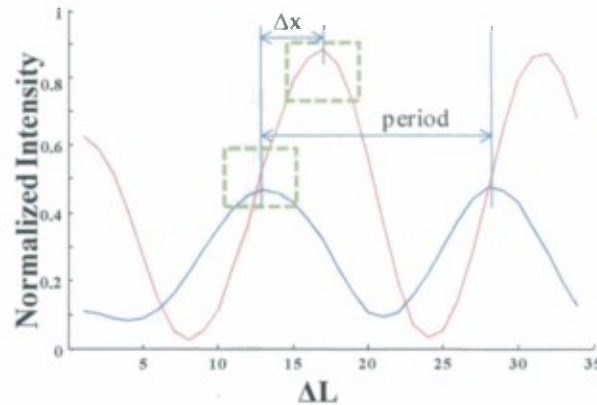
Figure 40 *Intensity of the reference (red) and MM (blue) beam spots plotted with respect to changes in the reference arm length during transmission measurement.*

The electric field of the MM beam 'spot' on the IR camera can be expressed as follows:

$$\vec{E} = \vec{E}_o e^{-jkx} + T_S \vec{E}_o e^{-jk_0(x+\Delta l+\Delta s)} \tag{1}$$

31

where X= length of reference arm, Δl=difference of path length between Arm 1 and Arm 2, Δs=phase due to metamaterial, T_s= Transmission coefficient of sample.

Eq. 1 can be used to derive the following equation for the MM beam spot intensities as a function of the path length difference between the piezo controlled reference arm and the sample arm:

$$I_s = \frac{1}{2}c\varepsilon \left|E_o^2\right|\left(1 + \left|T_S^2\right| + 2\left|T_S\right|\cos(\Phi_s)\right) \tag{2}$$

where, $\Phi_s = k_o x + k_o \Delta l + \Delta s$.

It is evident from Eq. 2 that for a given wavelength, intensity should vary sinusoidally with respect to path length difference between the Arm 1 and Arm 2. The above is clearly reflected in Fig. 7 which depicts actual intensities of the MM and reference beam spots for a particular wavelength with respect to the piezo controlled Arm 2 positions for a sample during t measurements.

Eq. 2 can be used to express the maxima and minima of the intensity values as follows:

$$I_{max} = \frac{1}{2}c\varepsilon \left|E_o^2\right|(1 + \left|t_S\right|)^2 \tag{3}$$

$$I_{min} = \frac{1}{2}c\varepsilon \left|E_o^2\right|(1 - \left|t_S\right|)^2 \tag{4}$$

Eq. 3 and Eq. 4 can be used to obtain the following expression for the transmission coefficient:

$$\left|t_S\right| = \frac{\sqrt{\frac{I_{max}}{I_{min}}} - 1}{\sqrt{\frac{I_{max}}{I_{min}}} + 1} \tag{5}$$

The reflection coefficient is acquired using a similar formalism developed above.

The reference beam spot intensity as a function of change in reference arm position can be expressed as follows:

$$I_{sub} = \frac{1}{2}c\varepsilon \left|E_o^2\right|\left(1 + \left|t_{Sub}^2\right| + 2\left|t_{Sub}\right|\cos(\Phi_{sub})\right) \tag{6}$$

where, $\Phi_{sub} = k_o x + k_o \Delta l$ and t_s= Transmission coefficient of substrate.

A comparison of the cosine terms in Eq. (2) and Eq. (6) makes it evident that the phase lag between the MM and the reference beams is exclusively due to the phase brought about by the metamaterial (Δs). Thus, the phase measurements for transmission and reflection are done by calculating the shift in the intensity versus change in Arm 2 position plots for the MM spot with respect to the reference beam spot. This shift is clearly observable in Fig. 7. Given the fact that the metamaterial curve is trailing the substrate curve, the metamaterial sample is bringing about a negative phase. The magnitude of this phase value can be expressed as follows, in terms of the nomenclature established in Fig. 7:

$$\Delta s = \frac{\Delta x}{period} \times 360^\circ \tag{7}$$

For accurate phase measurements, it is important that one performs 'reference' measurements for both transmission and reflection modes. This involves a scan without a sample present in Arm 1 prior to measuring a sample. This ensures that phase accrued due to geometric path length differences between the sample and substrate beams are accounted for.

The complex transmission and refection values obtained from the sample were used to find the refractive index and characteristic impedance using the following equations [1, 2]:

$$\hat{z} = X \pm \sqrt{X^2 + \frac{1}{n_s}} \qquad (8)$$

$$\hat{n} = \frac{1}{k_o d} \cos^{-1}[\frac{1 - \hat{r}^2 + n_s \hat{t}^2}{(n_s + 1)\hat{t} + \hat{r}\hat{t}(n_s - 1)} \qquad (9)$$

where n_s= refractive index of substrate, d=thickness of metamaterial and

$$X = \frac{i}{2n_s \sin(\hat{n}k_o d)}[\frac{2\hat{r}}{\hat{t}} + (n_s - 1)\cos(\hat{n}k_o d)]$$

From the complex refractive index values calculated above, one can calculate the effective permittivity ($\varepsilon = \hat{n}/\hat{z}$) and permeability ($\mu = \hat{n}.\hat{z}$) values of the metamaterial.

4.8 Results

In **Figure 41**, a graph has been provided which presents the experimentally obtained transmittance and reflectance values overlapped with those obtained from the simulations. One can observe resonance in the wavelength ranges of between 1450-1500nm for both the experimental and the simulated data.
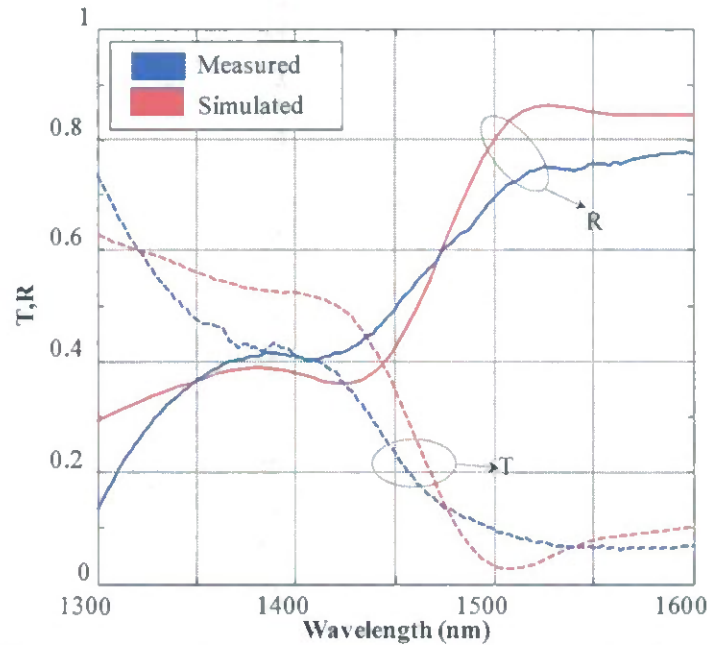

Figure 41 *(a) Measured and simulated transmittance (T) and reflectance (R) values.*

33

In Fig. 9 the real and imaginary parts of the simulated and measured effective permittivity and permeability values have been provided. The measured data clearly indicate that the real parts of both the measured permittivity and permeability values are simultaneously negative around 1450nm as predicted by the simulation results. Thereby the fabricated devices are double negative.
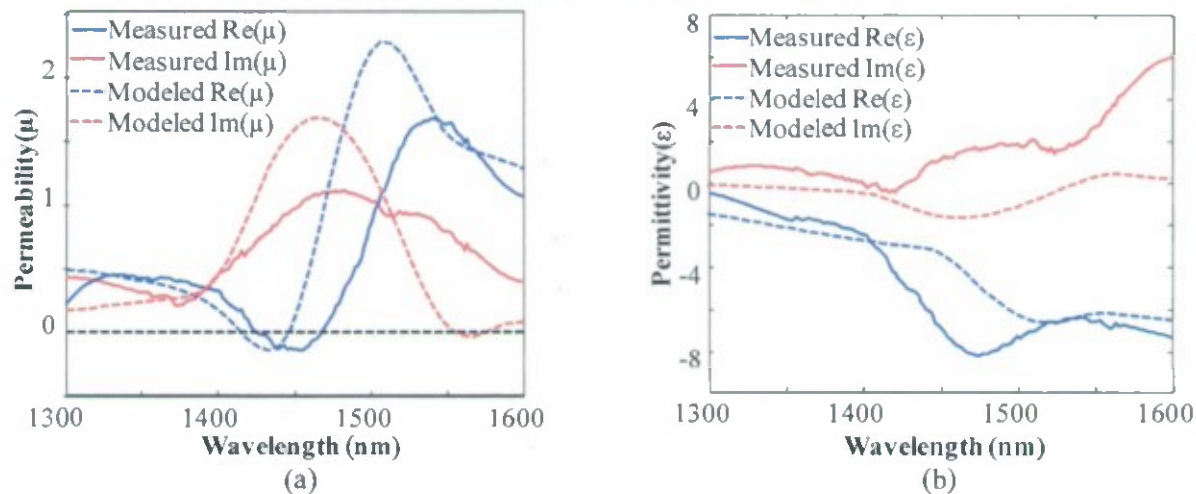

Figure 42 *(a) Simulated and measured μ. (b) Simulated and measured ε.*

The refractive index values for the measured and simulated structure are provided in **Figure 43**. A peak negative refractive index value of ~-2.5 can be observed. The remarkable similarity between the simulated and measured data is also evident.
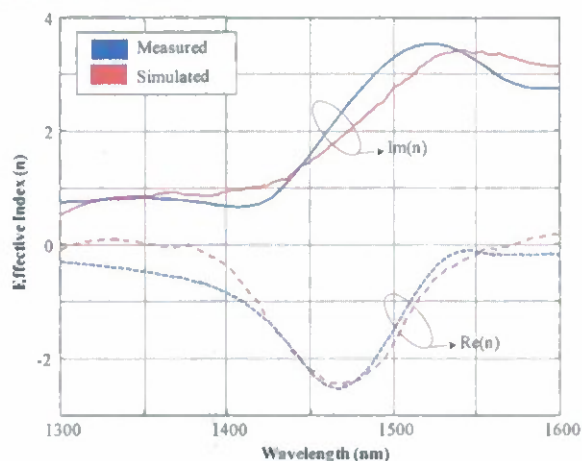

Figure 43 *The simulated and measured effective refractive index (n) values for the fabricated structure.*

In Fig. 11 a plot of the simulated and measured figure of merit (FOM) values have been presented. The FOM, which is seen as a performance metric for negative index metamaterial structures, is the ratio of the real part of the refractive index with respect to its imaginary part. A high FOM signifies low loss. A peak FOM value of approximately 1.8 is expected from our simulation results at a wavelength of about 1450nm. The fabricated structure exhibits a peak FOM of about 1.5 at 1450nm. This compares favorably with similar devices reported elsewhere [5].
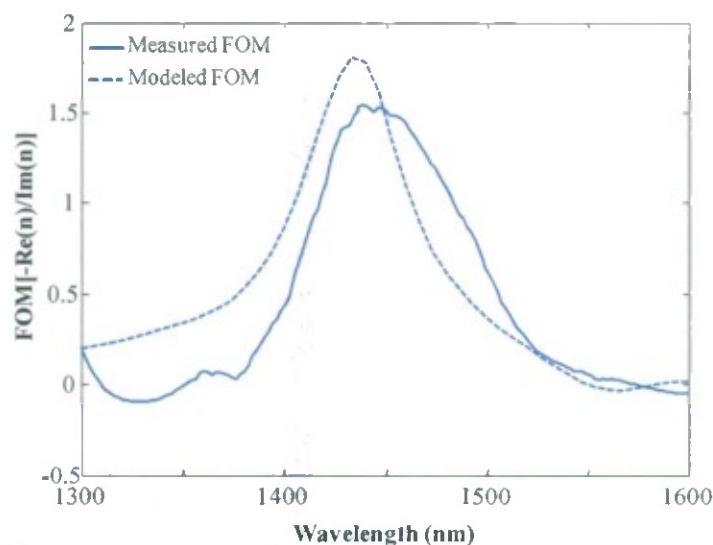
Figure 44. *Simulated and measured FOMs.*

The fabricated structures, as evident from **Figure 43** and **Figure 44**, exhibit differences in terms of their electric and magnetic behavior as compared to the simulation results. This is evident in the lower experimentally obtained peak negative values for the real part of ε as compared to those obtained from the simulated results. It is also evident that the imaginary part of the μ for the fabricated structure is somewhat lower which indicates lower magnetic losses in the fabricated samples near the resonant wavelengths as compared to simulated structure. However, the imaginary part of ε is higher in the fabricated structure as compared to the simulations. This indicates higher than expected electric loss. Nonetheless, the total optical loss in the fabricated sample, as evident from the imaginary part of **n** in Fig. 3.10, by and large matches that of the simulated structure. Thus, the higher than expected electric loss seems to be compensated for by the lower than expected magnetic loss.

There are a number of reasons which can lead to the above inconsistencies between the simulated and fabricated structures in terms of the electric and magnetic resonances. Firstly, the fabricated structures are slightly different in terms of the size and shape of the 'holes' as compared to the simulated structure. For instance, it is evident from Figure 39, that the fabricated structure features elliptical holes as opposed to the rectangular ones which were used for simulation. The elliptical shape of the 'holes' is brought by the diffraction effects during the DUV lithography process. The diffraction effects arise due the fact that the dimensions of the exposure mask patterns are comparable to the 220nm exposure wavelength. This results in rounding of the edges of the sacrificial template pillar structures which also leads in turn evident in the holes of the final structure. Furthermore, the lithography process and the ensuing etch procedures to form the sacrificial template have brought about further fabrication imperfections whereby 'hole' sizes vary randomly across the sample area. These variations in hole sizes can be as much as 50nm, both length and width wise, with respect to the simulated hole dimensions (400nm by 280nm). Thus, the 1mm diameter tunable laser output incident on the sample during the characterization process encounters a random array of 'unit cells' which differ slightly from one another in terms of their resonance characteristics around 1450nm. This brings about differences in the resonance characteristics between the simulated and measured structures.

5   Conclusion

The U.S. Navy has a vision of an integrated ship topside, where the elements detecting, guiding, processing, and radiating signals become an integral part of the ship's structure. To address these

requirements, we have used photonic crystals and meta-materials to construct a integrated signal detecting and processing system. The advantage of this approach over conventional techniques is that these devices are, to a large extent, electromagnetically transparent and therefore have a significantly reduced signature. The self-collimating PhC waveguide that is used as the basis of this system also offers very good signal isolation due to its low out-of-plane scattering and is energy efficient due to its low propagation loss. In addition, we designed I/O couplers that provide an efficient means to transfer electromagnetic energy to and from the PhC while producing a small signature. This effort also included the design of a spatial light modulator (SLM) based on tunable meta-materials. For our integrated design, this SLM allows us to process the detected signals while maintaining a low observable (LO) profile. Additionally, in our future work for this project we plan to implement a dielectric grating structure that will allow us to radiate a modulated signal from our integrated chip.

In summary, this integrated sensor chip incorporates a self-collimating PhC structure that is used to guide electromagnetic energy, with I/O dielectric waveguide couplers that provide a means to feed an integrated grating structure that will radiate electromagnetic energy through the tunable meta-material SLM to process the outgoing signals.

6   Publications for this project

1. I. O. Mirza, J. N. Sabas, S. Shi, and D. W. Prather, "Experimental demonstration of metamaterial-based phase modulation," *Progress In Electromagnetics Research*, PIER 93, 1-12, 2009.
2. I. O. Mirza, S. Shi, and D. W. Prather, "Phase Modulation Using Dual Split Ring Resonators," *Opt. Express* 17, 5089-5097 2009.
3. I. O. Mirza, S. Shi, D. W. Prather, "Metamaterial-based Tunable Phase Modulator," *Progress In Electromagnetics Research Symposium,* Moscow, Russia, August 2009.
4. J. N. Sabas, I. O. Mirza, S. Shi, and D. W. Prather, "An efficient self-collimating photonic crystal coupling technique in the RF regime," 7609-20, *Proc. SPIE Photonics West*, San Francisco, CA, 2010
5. Jerico Sabas, "Design And Fabrication Of Dispersion-Engineered Photonic Crystals for Applications in the Microwave Regime," Master's Thesis, 2010.
6. I. O. Mirza, J.N. Sabas, S. Shi, D. W. Prather, "Experimental Demonstration of Self-Collimating Photonic Crystals in the X-band Frequency." (*manuscript in progress*).
7. N. Dutta, S. Shi and D. W. Prather, "Fabrication of large area 3D 'fishnet' optical metamaterial structures", Waves in Random and Complex Media, **20: 2**, 289-297 (2010).
8. N. Dutta, I.O. Mirza, S. Shi, D.W. Prather, "Fabrication of Large Area Fishnet Optical Metamaterial Structures Operational at Near-IR Wavelengths", Materials, 3(12), 5283-5292 (2010).
9. N. Dutta, S. Shi, and D. Prather, "Large Area Near-IR Optical "Fishnet" Metamaterials," Proc. CLEO: CMV3 (2011).

7   References

1. **D. W. Prather,** et. al., *Photonic Crystals: Theory, Applications, and Fabrication.* Hoboken, NJ: John Wiley & Sons, 2009.
2. **I. O. Mirza**, J. N. Sabas, S. Shi, and D. W. Prather, "Experimental demonstration of metamaterial-based phase modulation," *Progress In Electromagnetics Research*, PIER 93, 1-12, 2009.
3. **I. O. Mirza**, S. Shi, and D. W. Prather, "Phase Modulation Using Dual Split Ring Resonators," *Opt. Express* 17, 5089-5097 2009.
4. **I. O. Mirza**, S. Shi, D. W. Prather, "Metamaterial-based Tunable Phase Modulator," *Progress In Electromagnetics Research Symposium*, Moscow, Russia, August 2009.
5. 1. D. W. Prather, et. al., *Photonic Crystals: Theory, Applications, and Fabrication.* Hoboken, NJ: John Wiley & Sons, 2009.
6. 2. J. N. Sabas, I. O. Mirza, S. Shi, and D. W. Prather, "An efficient self-collimating photonic crystal coupling technique in the RF regime," 7609-20, *Proc. SPIE Photonics West*, San Francisco, CA, 2010.
7. 3. Z. Lu, C. Schuetz, S. Shi, C. Chen, G. Behrmann and D. Prather, "Experimental demonstration of self-collimation in low-index-contrast photonic crystals in the millimeter-wave regime," *IEEE Transactions on Microwave Theory and Techniques,* Vol. 53, pp. 1362-1368, 2005.
8. Wu, W., et al., *Optical metamaterials at near and mid-IR range fabricated by nanoimprint lithography.* Applied Physics a-Materials Science & Processing, 2007. **87**(2): p. 143-150.
9. Zhang, S., et al., *Experimental demonstration of near-infrared negative-index metamaterials.* Physical Review Letters, 2005. **95**(13).
10. Venkataraman, S., et al., *Fabrication of three-dimensional photonic crystals using silicon micromachining.* Applied Physics Letters, 2004. **85**(11): p. 2125-2127.
11. Kim, T., et al., *Kinetics of gold nanoparticle aggregation: experiments and modeling.* J Colloid Interface Sci, 2008. **318**(2): p. 238-43.
12. Shalaev, V.M., *Optical negative-index metamaterials.* Nature Photonics, 2007. **1**(1): p. 41-48.